HAL
open science

Speciation and thermodynamic properties of La(III)-Cl complexes in hydrothermal fluids: A combined molecular dynamics and in situ X-ray absorption spectroscopy study

Qiushi Guan, Yuan Mei, Barbara Etschmann, Marion Louvel, Denis Testemale, Riccardo Spezia, Joël Brugger

To cite this version:

Qiushi Guan, Yuan Mei, Barbara Etschmann, Marion Louvel, Denis Testemale, et al.. Speciation and thermodynamic properties of La(III)-Cl complexes in hydrothermal fluids: A combined molecular dynamics and in situ X-ray absorption spectroscopy study. Geochimica et Cosmochimica Acta, 2022, 330, pp.27 - 46. 10.1016/j.gca.2022.02.032 . insu-03741359

HAL Id: insu-03741359

https://insu.hal.science/insu-03741359

Submitted on 1 Aug 2022

HAL is a multi-disciplinary open access archive for the deposit and dissemination of scientific research documents, whether they are published or not. The documents may come from teaching and research institutions in France or abroad, or from public or private research centers.

L'archive ouverte pluridisciplinaire **HAL**, est destinée au dépôt et à la diffusion de documents scientifiques de niveau recherche, publiés ou non, émanant des établissements d'enseignement et de recherche français ou étrangers, des laboratoires publics ou privés.

Available online at www.sciencedirect.com

ScienceDirect

Geochimica et Cosmochimica Acta 330 (2022) 27–46

Geochimica et Cosmochimica Acta

www.elsevier.com/locate/gca

Speciation and thermodynamic properties of La(III)-Cl complexes in hydrothermal fluids: A combined molecular dynamics and *in situ* X-ray absorption spectroscopy study

Qiushi Guan [a,b,*], Yuan Mei [b], Barbara Etschmann [a], Marion Louvel [c], Denis Testemale [d], Riccardo Spezia [e], Joël Brugger [a,*]

[a] *School of Earth, Atmosphere and the Environment, Monash University, Clayton, VIC 3800, Australia*
[b] *CSIRO Mineral Resources, Kensington, WA 6151, Australia*
[c] *Institute for Mineralogy, WWU Muenster D-48149, Germany*
[d] *CNRS, Université Grenoble Alpes, Institut Néel, F-38000 Grenoble, France*
[e] *Laboratoire de Chimie Théorique, Sorbonne Université, UMR 7616 CNRS, 4, Place Jussieu, 75005 Paris, France*

Received 31 August 2021; accepted in revised form 28 February 2022; Available online 7 March 2022

Abstract

Chlorine is the most common ligand in geofluids, and one of the most important complexing agents for rare earth elements. The geometry and thermodynamic properties of La(III)-Cl complexes determined by previous experimental studies show inconsistency especially at temperature over 350 °C. Here, *ab initio* molecular dynamics (MD) simulations were employed to determine the nature and thermodynamic properties of La(III)-Cl complexes at temperature up to 500 °C and pressure up to 30 kbar. The simulations were ground proofed by *in situ* X-ray absorption spectroscopy (XAS) results (400 bar, 25 to 500 °C). Both MD and XAS show an increase in the relative stabilities of chloride complexes with increasing temperature. The formation constants of $LaCl_n^{3-n}$ (n = 1–3) complexes were calculated using trmodynamic integration method that is within *ab initio* MD. The calculated formation constants of $LaCl^{2+}$ and $LaCl_2^+$ at temperatures below 400 °C agree with Migdisov et al.'s (2009) extrapolations from the Helgeson-Kirkham-Flowers (HKF) equation-of-state. We fitted the HKF equation-of-state parameters of $LaCl_n^{3-n}$ (n = 1–3) within the Deep Earth Model (DEW, Sverjensky et al., 2014) to enable the calculations of the formation constants up to 1200 °C, 60 kbar, based on the previous experimental data and the new results. The predictions confirm the increased stability of chloride complexes with increasing temperature and further underline the effect of pressure on La speciation: while $LaCl_3$(aq) becomes important in Cl-rich metamorphic and magmatic hydrothermal fluids (T > 350 °C; P < 5kbar) circulating in the upper crust, $LaCl^{2+}$ and $LaCl_2^+$ appear to be the dominant complexes under higher pressure characteristic of the lower crust or subducting slab environments.
© 2022 The Author(s). Published by Elsevier Ltd. This is an open access article under the CC BY-NC-ND license (http://creativecommons.org/licenses/by-nc-nd/4.0/).

Keywords: Rare earth elements; *Ab initio* molecular dynamics; Thermodynamic properties

1. INTRODUCTION

Rare earth elements (REE), including lanthanides, yttrium and scandium, are classified as critical metals (Hatayama and Tahara, 2015; Fortier et al., 2018;

* Corresponding authors at: School of Earth, Atmosphere and the Environment, Monash University, Clayton, VIC 3800, Australia and CSIRO Mineral Resources, Kensington, WA 6151, Australia (Q. Guan).

E-mail addresses: qiushi.guan@csiro.au (Q. Guan), joel.brugger@monash.edu (J. Brugger).

https://doi.org/10.1016/j.gca.2022.02.032
0016-7037/© 2022 The Author(s). Published by Elsevier Ltd.
This is an open access article under the CC BY-NC-ND license (http://creativecommons.org/licenses/by-nc-nd/4.0/).

Australian Critical Minerals Prospectus 2020) due to increasing demand and the potential of their supply being at risk (Skirrow et al., 2013; Ram et al., 2019; González-Álvarez et al., 2021). The chemical properties of lanthanides are fundamentally similar, with slight differences governed predominantly by differences in ionic radii, that decrease with increasing atomic number; therefore, aside from their increasing relevance to support transition away from fossil fluids, REE serve as geological tracers in a wide range of geological environments, from high temperature magmatic to the low temperature environment (Brugger et al., 2008; Migdisov et al., 2016).

Although magmatic processes play a key role in the formation of primary REE deposits, REE are mobile in hydrothermal fluids, and hydrothermal processes often control the mineralogy and grade distribution of the deposits (e.g., Bayan Obo, China; Ling et al., 2013; Gallinas Mountains, New Mexico; Williams-Jones et al., 2000; Thor Lake, Canada; Sheard et al., 2012). In such contexts, metal mobility is controlled by the formation of aqueous complexes, whose nature vary with temperature, pressure and the chemical composition of the fluid (Brugger et al., 2016). Understanding the behaviour of REE under hydrothermal conditions is thus necessary to improve geological models of REE deposit formation and supporting innovation in mineral exploration; this knowledge also underpins the development and optimisation of hydrometallurgical routes of REE recovery.

Lanthanum is the first element of the lanthanides (Ln) and is categorized as a light REE (LREE). It is usually concentrated with Ce in monazite or bastnaesite (Smith and Henderson, 2000). Although LREE are expected to form stronger complexes with fluoride than with chloride with increasing temperature (T > 250 °C, Migdisov et al., 2009), chloride is considered to be the main transporter of REE at high T because of its high availability in most geo-fluids, whereas the solubility of F is limited by phases such as fluorapatite and biotite (Migdisov et al., 2009; Xing et al., 2018). A number of experimental and theoretical studies have been conducted to determine the properties of the La(III) aqua ion and La(III)-chloride complexes, mostly at room temperature, i.e. hydration and chlorination numbers, coordination geometry, and thermodynamic properties (Table 1). The hydration numbers of the Ln(III) aqua ions remained controversial for a long time, with values between 8 and 12 reported by different authors for La (III)-O distances of 2.48–2.72 Å (references in Table 1; van Sijl et al., 2009). In the past decade, a consensus has been reached that the hydration structure of the La(III) aqua ion at room temperature is a tricapped trigonal prism with 9 water molecules (D'Angelo and Spezia, 2012 and reference therein). Only one study has investigated the coordination of the La(III) aqua ion at elevated temperature (Anderson et al., 2002). The results suggest a change in coordination geometry reflected by a split of the La(III)-O distances (Table 1), but do not show a significant decrease in the hydration number, as is generally observed under hydrothermal conditions (Brugger et al., 2016).

Several studies were also conducted on the structure of aqueous La(III)-Cl complexes at room temperature. Combining Raman spectroscopy and Density Functional Theory (DFT), Rudolph and Irmer (2015) found that minor amounts of La(III) chloro-complexes ($[La(H_2O)_{9-n}Cl_n]^{3-n}$, with n = 1 and 2) form in concentrated $LaCl_3$ solutions (3.05 molar (M) and 2.03 M; below detection in 0.051 M), but found significant amounts of La(III) chloro-complexing ($[La(H_2O)_{9-n}Cl_n]^{3-n}$, with n = 1–3) in solutions where 1 M or 4 M HCl were added. In contrast, Allen et al. (2000)'s EXAFS study identified chloride complexing only in the most concentrated solution (14 M LiCl), with an average coordination of La(III) corresponding to $[La(H_2O)_{6.5}Cl_{2.1}]^{0.9+}$. Beuchat et al. (2010)'s MD study determined an average coordination of $[La(H_2O)_{7.9}Cl_{0.8}]^{2.2+}$ in a 5 M Cl solution. In another MD study, Bühl et al. (2012) calculated equilibrium constants (logβ) for the formation of $LaCl^{2+}$ to be −1.9 (from a Helmholtz free energy of 2.6 (±0.9) kcal/mol for the reaction $La^{3+} + Cl^- = LaCl^{2+}$), indicating weak association at room temperature. The MD studies of Petit et al. (2008) and Bühl et al. (2012) also showed that a total coordination of eight was more stable than that of nine when Cl was bonding with La(III). Mayanovic et al. (2009) performed the only *in situ* experimental study of La(III) hydration and chloride complexing up to high temperature via EXAFS. They found that in a 0.02 molal (m) $LaCl_3$ + 0.06-m HCl solution, the number of bonded chlorides increases from below detection limit at room temperature, to 1.5 ± 0.6 at 150 °C, and to 3.1 ± 0.7 at 500 °C, 5.2 kbar. Concurrently, the measured hydration number decreased from 10.5 ± 1.4 at 25 °C to 3.8 ± 0.7 at 500 °C, corresponding to an overall reduction in coordination number of 3.6 ± 1 from 25 °C to 500 °C.

The thermodynamic properties for the formation of the $LaCl^{2+}$ and $LaCl_2^+$ complexes are well constrained at room temperature (review in Migdisov et al., 2016); for example, Luo and Byrne (2001) reported a formation constant (logK) of 0.65 for $REECl^{2+}$ at zero ionic strength. In the absence of high temperature experiments, early studies of hydrothermal REE transport were based on empirical extrapolations from room-temperature data; key studies include Wood (1990) (isocolumbic approach), and Haas et al. (1995) (Helgeson-Kirkham-Flowers (HKF) model; Shock and Helgeson, 1988). Solubility experiments by Gammos et al. (2002) and Migdisov et al. (2009), conducted up to 300 °C at saturated pressure (P_{sat}), provide the basis of our current understanding of REE-chloride complexing in hydrothermal fluids, with temperature-dependent formations constants for the $REECl^{2+}$ and $REECl_2^+$ complexes. However, Migdisov et al. (2016) suggested that the reliable use of the data for LREE(III)-Cl complexes should be limited to 350 °C. Indeed, the modelled REE(III)-Cl speciation using data from Migdisov et al. (2009) differs significantly from the *in situ* XAS studies of Mayanovic et al. (2009), especially for LREE (Migdisov et al., 2016): the average La(III)-Cl coordination numbers from Mayanovic et al. (2009) and Migdisov et al. (2016) are 1.5 ± 0.6 vs 0.46 at 150 °C; 2.2 ± 0.7 vs 1.33 at 300 °C; 2.6 ± 0.8 vs 1.66 at 400 °C; and 3.1 ± 0.7 vs 1.84 at 500 °C.

In this study, we employed *ab initio* MD together with *in situ* XAS measurements to provide comprehensive geom-

Table 1
Previous studies on the structure (hydration and stoichiometry) of the La(III) aqua ion and chloride complexes.

Reference	Method*	Solution**	N_O, N_{Cl}, or CN_{tot}	La-O or La-Cl distances (Å)	
Smith and Wertz, 1975, 1977	XRD	1.54–2.95 m $LaCl_3$	8.0(2)	2.48	RT
Habenschuss and Spedding, 1979	XRD	3.808 m $LaCl_3$	9.13(10)	2.58(1)	RT
Johansson and Wakita, 1985	XRD	0.7 M La + 1.16 M SeO_4^{2-}	8.0(3)	2.570(5)	RT
		2.88 M La + 9.16 $MClO_4^-$	8.0(3)	2.560(5)	
Marques et al., 2001	XRD, EXAFS, Raman	0.46 – 3.4 m of $LaCl_3$	6 (O_{prism}) / 3(O_{eq}); $CN_{tot} = 9$ (fixed)	2.560(9)/2.727(13)	RT; fits with two different models.
			8.2 (fixed)	2.549(17)	
Anderson et al., 2002	XAFS	0.007 m La in HNO_3	8.3(10)	2.59(2)	RT
			8.1(6)	2.60(2)	100 °C
			5.4(13) (O_{prism}) / 3.7(7) (O_{cap})	2.60(2)/2.71(0)	200 °C
			5.7(9) (O_{prism}) / 2.9(21) (O_{cap})	2.48(2)/2.79(6)	300 °C
Solera et al., 1995	EXAFS	0.05–0.2 M $LaCl_3$	12.0(5) (O)	2.56(1)	RT
Ishiguro et al., 2002	EXAFS	0.8 M $La(ClO_4)_3$	9	2.545(2)	RT
Allen et al., 2000	EXAFS	0.1 M La + 0.25 M HCl	9.2 (no chloride)	2.54	RT
		0.1 M La + 14 M LiCl	6.5 (O) / 2.1 (Cl); $CN_{tot} = 8.6$	2.57/2.92	RT
Näslund et al., 2000	EXAFS, LAXS	0.662 M $La(ClO_4)_3$	6 (O_{prism}) / 3(O_{eq})	2.515(8)/2.64(2)	RT
D'Angelo et al., 2008; Persson et al., 2008	EXAFS	0.2 M $La(H_2O)_9(CF_3SO_3)_3$	6 (O_{prism})	2.514(7) (L_3-edge); 2.579 Å (K-edge).	RT
			3(O_{eq})	2.640(9) (L_3-edge); 2.641 Å (K-edge).	
Ikeda et al., 2005	MD	1 $LaCl_3$ in 64 water	8/8.5		RT
Terrier et al., 2010	DFT	1 La(III) ion with 64 waters	9	2.58	RT
Díaz-Moreno et al., 2011	ND, XRD, EXAFS, EPSR	1 m $LaCl_3$	8 (O) / 1(Cl)	2.53 / 2.8	RT
Rudolph and Irmer, 2015	DFT, Raman	3.05 M/2.03 M/0.051 M $LaCl_3$	6 (O_{prism}) / 3(O_{eq}); $CN_{tot} = 9$	2.56/2.576	RT
		2.03 M $LaCl_3$ + 1 M/4M HCl	1 to 3Cl; $CN_{tot} = 9$		
		1.017 M $LaCl_3$ + 1 M/4M HCl			
Petit et al. 2008	MD	La(III) in 14 M LiCl	6.2 (O) / 2 (Cl); $CN_{tot} = 8.2$	2.55 / 2.88	RT
Beuchat et al., 2010	MD	0.05 M $LaCl_3$	9.1 (O)	2.66(27)	RT
		5 M $LaCl_3$	7.1 (O) / 0.8 ± 0.7(Cl); $CN_{tot} = 7.9$	2.54(27)/2.9(11)	
Bühl et al., 2012	MD	1 La(III), 0–3Cl(-I), 52–80 water	9 (O)7 (O) / 1 (Cl)	2.65(13) 2.98(10) (Cl)	RT
Mayanovic et al., 2009	EXAFS	0.02 m $LaCl_3$ + 0.06 m HCl	10.5(14) (O) / <0.7 (Cl); $CN_{tot} = 10.5(14)$	Not reported	25 °C
			8.9(8) (O) / 1.5(6) (Cl)		150 °C
			7.1(7) (O) / 2.2(7) (Cl)		300 °C
			6.1(9) (O) /2.6(8) (Cl)		400 °C
			3.8(7) (O) / 3.1(7) (Cl); $CN_{tot} = 6.9(10)$	Not reported	500 °C, 5.2 kbar

RT = room temperature. *XRD, X-ray diffraction; LXAS, large angle X-ray scattering; EPSR, empirical potential structure refinement; DFT, density functional theory; XAFS, X-ray absorption fine structure; ND, neutron diffraction; MD, molecular dynamics; EXAFS, extended X-ray absorption fine structure. **m, molality; M, molarity.

etry and stability information on La(III)-Cl complexes from 200 to 500 °C and from 400 bar to 30 kbar. The combination of MD coupled with XAS provides a powerful tool to underpin the speciation and geometry of metals in fluids (D'Angelo and Spezia, 2012; Brugger et al., 2016; Mei et al., 2015a, 2015b, 2016). Moreover, previous studies also showed that MD is able to provide accurate results at high P-T (e.g., to 1000 °C and 5 kbar, Mei et al., 2014; 800 °C, 13 kbar to 45 kbar, Stefanski and Jahn, 2020). Formation constants of $LaCl_n^{3-n}$ (n = 1, 2, 3) complexes were estimated using the *ab initio* thermodynamic integration method. Based on the new and literature results, Helgeson-Kirkham-Flowers equation-of-state parameters for La(III) chloro-complexes were fitted within the Deep Earth Model framework (DEW Model; Sverjensky et al., 2014), enabling extrapolations of data to a wide range of P-T conditions covering surface to magmatic hydrothermal to deep crustal or to subduction environments.

2. METHOD

2.1. *Ab initio* molecular dynamics

The *ab initio* MD simulations were conducted with Car-Parrinello Molecular Dynamics (CPMD, version 4.3, Car and Parrinello, 1985), using Kohn-Sham (Kohn and Sham, 1965) orbitals and a BLYP exchange correlation functional (Becke, 1988; Lee et al., 1988). To improve the structural and dynamic properties of water, the dispersion-corrected atom-centred pseudopotentials (DCACP) were used for the core electrons of oxygen and hydrogen atoms to account for the van der Waals interactions. Previous studies showed that accounting for the London dispersion forces improves the agreement between predicted and measured values of the water, e.g. radial distribution functions, metal/ion hydration, and thermophysical properties among others (von Lilienfeld et al., 2004; Lin et al., 2009; D'Angelo et al., 2010; Bankura et al., 2014; Priyadarsini et al., 2020).

Troullier-Martins norm-conserving pseudopotentials (Troullier and Martins, 1991) were used for all atoms. For La, the pseudopotential was generated from the reference configuration $5s^2 5p^6 5d^0 4f^0$ (PP1 from Terrier et al. 2010), with a plan-wave cut-off at 110 Ry. The Kleinman-Bylander scheme was applied (Kleinman and Bylander, 1982) with p as the local parts of the pseudopotential. A timestep of 3 a.u. (0.073 fs) and a fictitious electron mass of 400 a.u. were used in the simulations. The temperature was controlled with the Nosé-Hoover chain thermostat for ions and electrons. Periodic boundary conditions were applied to eliminate surface effects. The densities of the simulated solutions were chosen according to the equation of state of $NaCl_{(aq)}$ at a similar chloride concentration as the targeted T and P conditions (Driesner, 2007; Driesner and Heinrich, 2007). The canonical ensemble (NVT) was applied to conduct the simulations. The details of the atoms contained in the simulations, the boxes size, density, and the T and P conditions of each run are summarized in Table 2. The MD simulations were conducted for 16–36 ps, with an additional 2 ps initial equilibration, which proved to be sufficient to achieve reproduceable and meaningful results for aqueous simulations (e.g., Liu et al., 2013; Mei et al., 2020; Stefanski and Jahn, 2020). The time-averaged radial distribution functions (RDF) and the coordination numbers (CN) were calculated from the trajectories with VMD (Humphrey et al., 1996). Debye-Waller factors were calculated following equations in section 2.3 in Campbell et al. (1999). The Debye-Waller can only be calculated when no ligand exchange was observed during the simulation.

2.2. *Ab initio* thermodynamic integrations

As discussed in our previous studies (Mei et al., 2014, 2016; Guan et al, 2020), it is not practical to measure the relative stability of different complexes via *ab initio* MD given the limited ranges in simulation times and box sizes dictated by finite CPU resources. Several experimental studies have measured the residence times of water in $HREE^{3+}$ aqua ions (Cossy et al., 1989; Helm and Merbach 1999; 2002; Richens 2005); however, few values are available for LREE as higher magnetic fields are required for those Nuclear Magnetic Resonance measurements. (Helm and Merbach, 1999; Clavaguéra et al., 2005). The water residence time of Pr(III) was determined to be up to 2.5 ns (Powell and Merbach, 1994), and the values for La(III) are expected to be longer (Helm and Merbach, 1999). No experimental data is available for the residence times of Cl in REE^{3+} complexes; for comparison, residence times of transition metals complexes are in the ms-range, at 9.3 ms (Au(III)), 251 ms (Zn(III)) and < 32 ms (Cd(III)). (Sharps et al., 1993). Although the ligand exchange kinetics increases with temperature, leading to a decrease of ligand/water residence time, and making it possible to observe these exchanges via unconstrained *ab initio* MD simulations, it is generally not achievable to quantitatively determine the relative stability of different species from their statistical distributions during the simulations. To circumvent this issue and obtain quantitative information regarding ion association/dissociation, we used *ab initio* thermodynamic integration (Sprik, 1998; Sprik and Ciccotti, 1998) to calculate the free energy of ligand exchange reactions of La(III)-Cl complexes. The method is based on the fact that free energies of reactions are independent of the reaction path, and uses distance constraints to measure the forces required to transform an initial to a final configuration along a predefined reaction path (Guan et al., 2020). In this study, the La(III)-Cl distances (r) were constrained, and the mean constrained force ($f(r)$) required to maintain the La(III)-Cl distance at r was calculated by sampling all the possible aqueous configurations of La(III) at each r.Sufficient sampling required at least 8 ps simulation. For example, in the dissociation reaction:

$$LaCl^{2+} = La^{3+} + Cl^- \quad (1)$$

the initial La(III)-Cl distance r_I was chosen according our *ab initio* MD simulations in section 3.1, which represents the equilibrium bond distance at each P-T condition; the final La(III)-Cl distance r_F was chosen as there were no

Table 2
Ab initio MD simulation details.

Box No.	composition	T (°C)	P (bar)	Box size (Å)	Density (g/cm^3)
1	55 H_2O, La, 3 Cl	200	400	12.24	1.12
		300	400	12.89	0.96
		300	5 k	12.11	1.16
		300	8 k	11.89	1.22
		300	10 k	11.79	1.25
		300	20 k	11.47	1.36
		300	30 k	11.35	1.40
		400	400	13.67	0.80
		500	500	14.72	0.64
		500	5 k	12.57	1.03
		500	10 k	12.09	1.16
2	55 H_2O, La, 5 Cl, 2Na	200	400	12.59	1.13
		400	400	13.60	0.89
		500	600	14.37	0.76
3	111 H_2O, La, 5 Cl, 2Na	200	400	15.68	1.02
		400	400	17.34	0.75
		500	600	18.83	0.59

interactions between Cl^- and the La(III) complexes (i.e., $f(r_F) \approx 0$). The Helmholtz free energy of reaction (1) can be calculated by (Sprik and Ciccotti, 1998; Sprik, 2000):

$$\Delta A_{I\to F} = -\int_{r_I}^{r_F} f(r)dr \tag{2}$$

Details of the step-by-step thermodynamic integration are described in section 3.2. The Gibbs free energy of the reaction was approximated as $\Delta_r G = \Delta A_{I\to F}$, as the energy contribution caused by pressure change is negligible (Mei et al., 2013, Mei et al., 2015a). The standard Gibbs free energy of each reaction at infinite dilution ($\Delta_r G^{\Theta}$) was calculated from $\Delta_r G$ with concentration and activity corrections (Mei et al., 2013), using activity coefficients calculated via the B-dot extension of the Debye-Hückel theory (Helgeson et al., 1981). The concentrations of the species were defined with the initial (distance r_I; reactants) and final positions (r_F; products) in the *ab initio* thermodynamic integration, given the fact that the results are independent of the reaction path. For example, for reaction (1), the simulation box at distance r_I contains 1 m $LaCl^{2+}$ + 2 m Cl^-; and at distance r_F it contains 1 m La^{3+} + 3 m Cl^-. Finally, the formation constant (K) was obtained from

$$\Delta_r G^{\Theta} = -RT\ln K \tag{3}$$

where R is the gas constant and T is temperature in Kelvin. The stepwise formation constants of the reactions $LaCl_{n-1}^{3-n+1} + Cl^- = LaCl_n^{3-n}$, with n = 1–3 were calculated using *ab initio* thermodynamic integration, and cumulative formation constants (logß) for each complex (reactions $La^{3+} + nCl^- = LaCl_n^{3-n}$; n = 1 – 3) were obtained from the sum of the stepwise formation constants:

$$log\beta_n(LaCl_n^{3-n}) = \sum_1^n logK_n(LaCl_n^{3-n}) \tag{4}$$

The uncertainties of $\Delta_r G$ and logK were estimated following the method described in section 6.4 of Allen and Tildesley (1987), and include both systematic and statistical errors. This method has been used to estimate the uncertainty of thermodynamic integration in previous studies (e.g., Rodinger et al., 2005; Mei et al., 2018; 2020; Guan et al., 2020).

2.3. X-ray absorption spectroscopy

Experimental solutions for *in-situ* XAS measurements were prepared by dissolving the appropriate amounts of solids in acidified water. The compositions of the solutions are listed in Table 3. Note that due to the high absorption of X-rays by NaCl at the La L_3 edge (5483 eV), LiCl was used for high salinity measurements. Analytical grade lanthanum oxide (La_2O_3), lithium chloride (LiCl), 37 % HCl and MilliQ water were used to prepare the solutions.

The speciation of La(III) in Cl-rich fluids was characterised via *in situ* X-ray absorption measurements (XAS) using the high temperature-high pressure cell developed at the Institut Néel/ESRF (Bruyère et al., 2008; Testemale et al., 2005). This cell consists of an external water-cooled pressure vessel equipped with three beryllium windows enabling collection of simultaneous fluorescence and transmission signals. The sample is contained inside a glassy carbon tube with an internal diameter of 4 mm that is placed inside a small cylindrical resistive heater. Pressure is applied to the sample by two glassy carbon pistons, using helium as a pressure medium. Temperature is recorded by two thermocouples placed within the heating element. Although the thermocouples sit near the sample, they are placed outside the sample and the temperature of the fluid at the beam location is calibrated (e.g., Brugger et al., 2007; Etschmann et al., 2010; Liu et al., 2011; Louvel et al., 2017) by comparing the density of pure water calculated from measurements of the absorbance and X-ray mass attenuation coefficients tabulated by Chantler (1995) to that determined from the equation of state of pure water (NIST database, Lemmon et al., 2000). This method provides a direct measurement of the temperature at the beam position; temperature accuracy is better than 5 °C, and temperature varied within less that 1 °C during the measurements. Pressure was read from

Table 3
Compositions and maximum P-T conditions of solutions measured by *in situ* XAS.

Solution	Composition	Maximum T, P
Sol2	0.079 m La (as La_2O_3(s)) + 1.008 m HCl	450 °C, 400 bar
Sol9	0.088 m La ($LaCl_3$(s)) + 4.56 m LiCl + 0.183 m HCl (total chloride 5.011 m)	500 °C, 400 bar
Sol13	0.048 m La ($LaCl_3$(s)) + 0.003 m HCl (total chloride 0.147 m)	400 °C, 400 bar

a calibrated Bourdin gauge with a precision better than 5 bar; during the experiment, pressure was maintained with 1 bar by the PID system (Bruyère et al., 2008).

Lanthanum L_3-edge (5483 eV) Extended X-ray Absorption Fine Structure (EXAFS) spectra were collected up to 500 °C at 400 bar at the FAME beamline at the European Synchrotron Research Facility (ESRF) in Grenoble, France. Given the low energy of the La L_3 edge, it was necessary to minimise the amount of material in the beam path, hence experiments were limited to 400 bar and a maximum salinity of 4.5 m LiCl.

The ESRF is a 6.03 GeV ring, and operating in 7/8 multi-bunch mode it has a maximum current of 200 mA. FAME is a bending magnet beamline (see Proux et al., 2005 for details), and its double crystal Si(220) monochromator provides an energy resolution of 0.28 eV at the La L_3-edge energy. A focused beam size of FWHM 220x145 μm^2 was used. The incident and transmitted beam intensities I_0 and I_1 were measured with Si diodes, and a Canberra 30 element solid state fluorescence detector was used for detecting fluorescence data. The beam energy was calibrated such that the maximum of the first derivative was at 5483 eV.

EXAFS data were analysed with the HORAE package (Ravel and Newville, 2005), using FEFF version 9 (Rehr et al., 2009); E_0 was defined as the maximum of the first derivative. Reported errors in EXAFS parameters (1-σ) are those calculated by the Artemis program (part of HORAE).

EXAFS spectra represent a final state interference effect arising from the scattering of the outgoing photoelectron from neighbouring atoms, and are therefore mainly sensitive to the nature (atomic number), quantity and distance of the neighbouring atoms. The amplitude reduction factor (S_0^2) accounts for processes that contribute to the X-ray absorption coefficient but not to the EXAFS (Roy et al. 1997), and is determined by fitting a compound with similar molecular structure as the unknown. S_0^2 was determined by simultaneously fitting multiple standards, La_2O_3(s), LaF_3(s), $LaCl_3$(s) and $LaCO_3F$(s). A S_0^2 value of 1.0 was determined by refining the S_0^2, bond lengths and EXAFS Debye-Waller factors; this value is consistent with theoretical constraints (Roy et al. 1997) and was used in all subsequent refinements.

The LaOCl(s) structure (Hölsä et al., 1997, ICSD # 84330) was used to generate the O and Cl paths. For each solution, all spectra were fitted simultaneously, resulting in one ΔE_0 and one set of goodness-of-fit parameters for each solution (Table 5). The EXAFS Debye-Waller σ^2 was fitted at 25 °C for each solution, with the constraint that it should then double from 30 to 500 °C, as determined from MD simulations. Note that the EXAFS Debye-Waller values determined from the *ab initio* MD simulations are higher than the experimental ones, as a result of the short sampling times in *ab initio* MD, that tend to overestimate structural disorder. However, the *relative* changes in fitted EXAFS Debye-Waller values are likely to be accurate, especially since the vibrational characteristics of the complexes are well reproduced by *ab initio* MD (e.g. Mei et al., 2013 and references therein). In practice this was applied by increasing the EXAFS Debye-Waller by a factor of 1.2 for each ~100 °C increase in temperature. The EXAFS Debye-Waller for Cl^- was defined to be the same as that for O, in part to reduce the number of variables and in part due to the (usually) low Cl:O ratio.

3. RESULTS

3.1. Geometry and nature of La(III)-Cl complexes

3.1.1. ab initio MD

The *ab initio* MD simulations were conducted at temperatures from 200 °C to 500 °C, and pressures from 400 bar to 30 kbar (Table 2). The *ab initio* MD simulation results are summarized in Table 4, and the snapshots of different La (III)-Cl complexes are presented in Fig. 1.

Overall, with increasing T, both the total coordination number (CN_{tot}) and the hydration number of La(III) decrease, while the chloride coordination number increases. At 200 °C, 400 bar, CN_{tot} was ~8 for La(III) coordinated with either one (jobs 1a, 3a) or two (job 2a) Cl^- at distances of 2.86 – 2.92 Å.

At 400 °C, 400 bar, in boxes 1 (job 1h) and 2 (job 2b), three Cl^- were bonded to La(III). The hydration numbers were close in both cases, 3.9 in job 1h and 3.6 in job 2b. The first appearance of La(III) bonding to 4 Cl^- was observed at this temperature in simulation 3b, in which the average CN of Cl^- was 3.4; this correlates with a decrease in hydration number to 2.8.

The trend of increasing bonding with Cl^- as a function of temperature was confirmed by the simulations at 500 °C, 600 bar (job 1i, 2c and 3c). The hydration number decreased with increasing number of bonded Cl^-: in job 1i, 3c and 2c, the hydration numbers were 3.5, 2.5 and 2, and the CN of Cl^- were 3, 3.4 and 4, respectively.

The MD results indicate that the hydration number also increases with increasing P under isothermal conditions. At 300 °C, the total CN of La(III) increased with increasing pressure from 400 bar to 30 kbar. From 400 bar to 8 kbar, the hydration number increased from 6.2 to 8.2 (jobs 1b, 1c and 1d) at distances of 2.59 – 2.57 Å, whereas the CN of Cl^- decreased from 1.7 to 0.4 at 2.82 – 2.89 Å. From 10 kbar to

Table 4
Ab initio MD results. Debye-Waller can only be measured when there is no ligand exchange in the simulation.

Box No.	Job No.	T (°C)	P (bar)	Simulation Time (ps)	Initial configuration	La-O		La-Cl			Total CN	Average species
						CN	r (Å)	CN	r (Å)	σ^2 (Å^2)		
1	1a	200	400	25.6	$[LaCl_2(H_2O)_7]^+$	7.2	2.55	1	2.86	0.0660	8.2	$[LaCl(H_2O)_{7.2}]^{2+}$
	1b	300	400	26.3	$[LaCl(H_2O)_6]^{2+}$	6.2	2.59	1.7	2.84		7.9	$[LaCl_{1.7}(H_2O)_{6.2}]^{1.3+}$
	1c	300	5 k	28.5	$[LaCl_2(H_2O)_6]^+$	7	2.58	1.2	2.82		8.2	$[LaCl_{1.2}(H_2O)_7]^{1.8+}$
	1d	300	8 k	35.8	$[LaCl(H_2O)_9]^{2+}$	8.2	2.57	0.4	2.86		8.6	$[LaCl_{0.4}(H_2O)_{8.2}]^{2.6+}$
	1e	300	10 k	28.5	$[LaCl_2(H_2O)_7]^+$	7.7	2.57	0.6	2.89		8.3	$[LaCl_{0.6}(H_2O)_{7.7}]^{2.4+}$
	1f	300	20 k	28.5	$[LaCl(H_2O)_8]^{2+}$	7.6	2.54	1	2.85		8.6	$[LaCl(H_2O)_{7.6}]^{2+}$
	1g	300	30 k	38.2	$[LaCl_2(H_2O)_8]^+$	8.6	2.57	0.3	2.89		8.9	$[LaCl_{0.3}(H_2O)_{8.6}]^{2.7+}$
	1h	400	400	24.8	$[LaCl_3(H_2O)_5]^0$	3.9	2.57	3	2.78	0.0376	6.9	$[LaCl_3(H_2O)_{3.9}]^0$
	1i	500	600	26.6	$[LaCl_3(H_2O)_5]^0$	3.5	2.58	3	2.76	0.0243	6.5	$[LaCl_3(H_2O)_{3.5}]^0$
	1j	500	5 k	32.0	$[LaCl_3(H_2O)_6]^0$	5.8	2.58	2	2.76		7.8	$[LaCl_2(H_2O)_{5.8}]^+$
	1 k	500	10 k	36.1	$[LaCl_3(H_2O)_6]^0$	6.4	2.56	1.5	2.83		7.9	$[LaCl_{1.5}(H_2O)_{6.4}]^{1.5+}$
2	2a	200	400	33.7	$[LaCl_3(H_2O)_6]^0$	6	2.57	2	2.92	0.0235	8	$[LaCl_2(H_2O)_6]^+$
	2b	400	400	22.3	$[LaCl_4(H_2O)_4]^-$	3.6	2.57	3	2.83	0.0194	6.6	$[LaCl_3(H_2O)_{3.6}]^0$
	2c	500	600	19.1	$[LaCl_5(H_2O)_2]^{2-}$	2	2.63	4	2.83	0.0234	6	$[LaCl_4(H_2O)_2]^-$
3	3a	200	400	18.9	$[LaCl(H_2O)_8]^{2+}$	7.1	2.59	1	2.91	0.0218	8.1	$[LaCl(H_2O)_{7.1}]^{2+}$
	3b	400	400	17.9	$[LaCl_3(H_2O)_5]^0$	2.8	2.62	3.4	2.73		6.2	$[LaCl_{3.4}(H_2O)_{2.8}]^{0.4-}$
	3c	500	600	16.8	$[LaCl_4(H_2O)_4]^-$	2.5	2.65	3.4	2.74		5.9	$[LaCl_{3.4}(H_2O)_{2.5}]^{0.4-}$

30 kbar, the hydration number increased from 7.7 to 8.6 Å at distance of 2.57 – 2.54 Å (job 1e, 1f and 1g), and the CN of Cl^- at each pressure was 0.6 (10 kbar), 1 (20 kbar) and 0.3 (30 kbar). At 500 °C, from 600 bar to 10 kbar (job 1i, 1j and 1k), the hydration number increased from 3.5 to 6.4 at distance of 2.56 – 2.58 Å, and the CN of Cl^- decreased from 3 to 1.5 at distance of 2.76 – 2.83 Å. The radial distribution functions of the simulations of box 1 are presented in Fig. 2.

3.1.2. La(III)-O coordination and bond length from in-situ EXAFS

The La EXAFS (k-space) and Fourier transformed (R-space) data and final fits are shown in Fig. 3, and the model parameters derived from the fits are tabulated in Table 5. The EXAFS data show a decreasing amplitude and a broadening of the oscillation between 2 and 4 Å^{-1} with increasing temperature. The multi-electron excitation peak, described previously for example by Solera et al (1995), is indicated by an arrow.

The classic dehydration effect of coordination complexes with increasing temperature (e.g., Brugger et al., 2016; Mei et al., 2015a) is exhibited in R-space: the magnitude of the peak in the radial distribution function decreases, and the peak position shifts to a longer distance with increasing temperature, consistent with decreasing total coordination numbers and increasing Cl:O ratio. This evolution is also seen in the fitted structural parameters (Table 5): the largest change is recorded in Sol9 (4.56 m LiCl + 0.183 m HCl), where the total ligand number decreased from 8.5 (30 °C) to 6.9 (500 °C), with the Cl:O ratio increasing from 0.0 to ~1.0.

Our fitted coordination numbers and bond lengths (Table 5) are comparable to previous studies (Table 1). The fitted La(III)-O coordination numbers ranged from 8.1(5) to 9.3(7) at room temperature, 400 bar, which is within error (2σ) of nine oxygen ligands coordinated to La. The fitted La(III)-O bond length (2.567(8) – 2.58(1) Å) is similar to previously noted La(III)-O bond lengths at ambient conditions (Table 1).

The number of coordinated oxygen ligands typically decreases with increasing temperature. The oxygen coordination number dropped from 8.5(6) at 30 °C to 3.5(5) at 500 °C in Sol9; this decrease is comparable with Mayanovic et al. (2009)'s study of a relatively dilute $LaCl_3$-HCl solution (Table 1). The EXAFS study by Anderson et al. (2002) did not record a decrease in La(III)-O coordination in the La(III) aqua ion between 25 °C and their maximum temperature of 300 °C. This is most similar to Sol13, which has the lowest La:Cl ratio of the solutions measured in this study: oxygen coordination number was 7.8(7) at 300 °C, and the total ligand coordination was 8.8(7), i.e. a similar total coordination number to that observed by Anderson et al. (2002).

With increasing temperature, our fitted La(III)-O bond lengths remain the same within error. The only other study to record La(III)-O bond lengths at higher temperatures (Anderson et al., 2002) noted a decrease from 2.59(2) to 2.48(2) Å for the 6 prism oxygen ligands and an increase from 2.59(2) to 2.79(6) Å for the 3 capping oxygens as

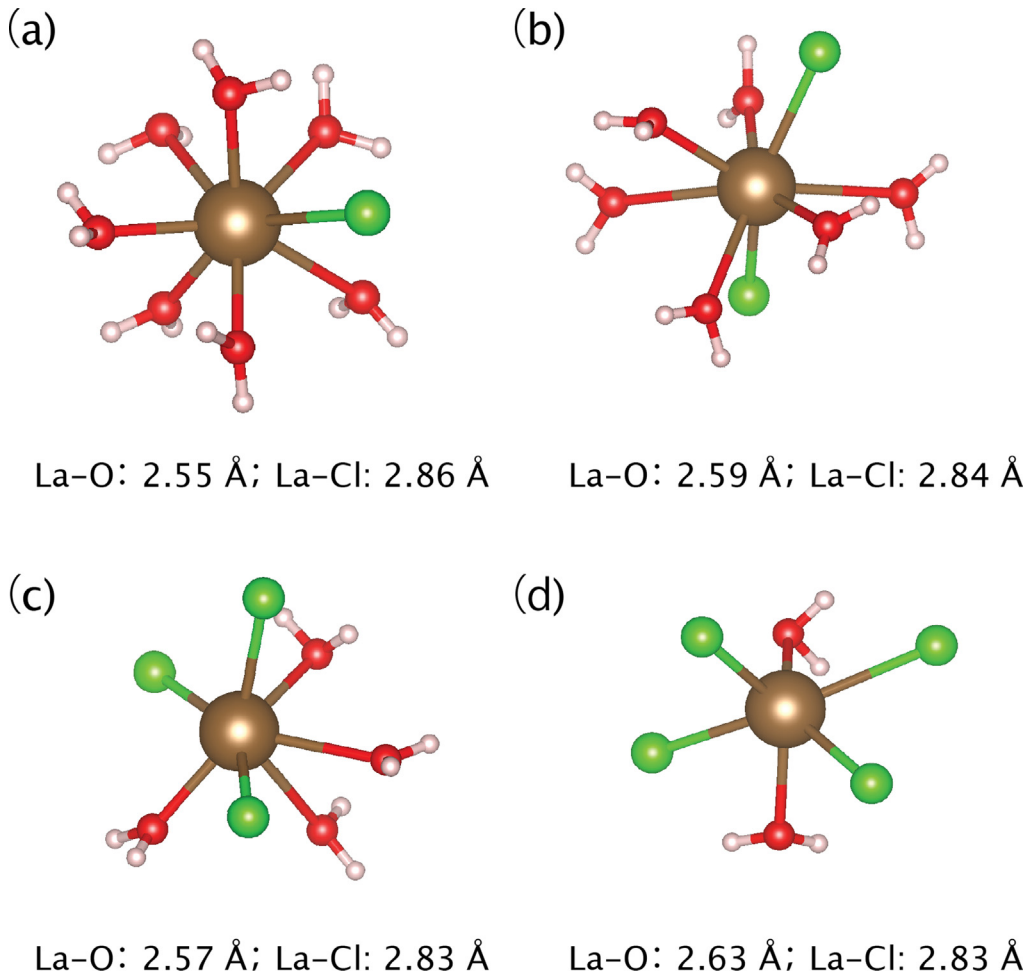

Fig. 1. Snapshots of La(III)-Cl^- complexes and the average bond distances. (a) $[LaCl(H_2O)_7]^{2+}$ from job 1a; (b) $[LaCl_2(H_2O)_6]^+$ from job 1b; (c) $[LaCl_3(H_2O)_4]^0$ from job 2b; (d) $[LaCl_4(H_2O)_4]^-$ from job 2c. Brown ball: lanthanum; red ball: oxygen; white ball: hydrogen; green ball: chlorine.

the temperature increased from room temperature to 300 °C, resulting in an average La(III)-O bond length of 2.58 Å at 300 °C.

3.1.3. La(III)-Cl coordination and bond length from in-situ EXAFS

It was difficult to fit the number of Cl unambiguously due to the fact that the La(III)-O and La(III)-Cl peaks overlap substantially and the data was noisy, due to the significant absorption of La Lα X-rays by the sample environment (solution and beryllium windows mainly). The large core hole of La combined with the noise in the data result in relatively large errors in the fits.

We note the unambiguous appearance of Cl^- in the first shell from 200 °C for the high Cl^- solutions and 300 °C for Sol13. Adding a fixed low number of Cl in some of the lower temperature solutions was warranted by the results of previous solubility studies (Migdisov et al., 2009), that noted the presence of La(III)-Cl coordination from ~ 200 °C. We found a maximum of 3.5(9) Cl^- within the first coordination shell of La(III) in Sol9 at 500 °C, which is similar to the 2–3Cl ligands noted in the studies of Allen et al. (2000), Petit et al. (2008) and Rudolph and Irmer (2015). Our fitted La(III)-Cl bond lengths range from 3.02(20) Å to 2.90(2) Å, within error of the EXAFS-derived La(III)-Cl distance of 2.91 Å from Allen et al. (2000), and close to the 2.88 Å determined by the combined classical and *ab initio* MD study of Petit et al. (2008).

3.2. *Ab initio* thermodynamic integration

The results from *ab initio* MD simulations and EXAFS fits in section 3.1 provide a qualitative knowledge of the coordination and geometry of La(III)-Cl complexes. However, the thermodynamic properties La(III)-Cl complexes are required to determine the relative stabilities and mobilities of La(III) in Cl-rich hydrothermal fluids. Both the unconstrained MD· and the experimental XAS results suggest the existence of $LaCl_4^-$ at high temperature (>400 °C) and high Cl-concentrations (≥5 molal). However, the chance of observing the $LaCl_4^-$ species is smaller than for $LaCl_3$(aq), except for MD job 2c (500 °C, 600 bar; ~5 molal Cl), in which the coordination number of Cl is 4. In the corresponding experimental solution (Sol9, ~5 molal Cl_{tot}, 500 °C), the Cl coordination number is 3.5 ± 0.9. Hence, we conclude that $LaCl_4^-$ could exist in some high salinity

Table 5
Results of fitting EXAFS data. n_O, n_{Cl} are the number of ligands coordinated to La, r_O, r_{Cl} are the La-O and La-Cl bond lengths. σ^2 is the EXAFS Debye-Waller factor. χ^2_{red} and R-factor are the goodness of fit parameters. All data were collected at 400 bar.

Sol2										
T (°C)	n_O	r_O (Å)	n_{Cl}	r_{Cl} (Å)	σ (Å^2)	E0 (eV)	χ^2_{red}	r-factor	k-range (Å^{-1})	R-range (Å)
30	8.1(5)	2.567(8)			0.005(1)	8.6(4)	120	0.015	2–8	1.3–3.1
200	7.5(9)	2.57(1)	0.5 (fix)	3.02(20)	0.008				2–8.5	1.3–3.1
300	6.9(6)	2.57(1)	1.0 (fix)	2.98(8)	0.009				2–8.1	1.3–3.1
350	6.2(5)	2.57(1)	1.3(5)	2.96(3)	0.009				2–8	1.3–3.1
400	5.6(6)	2.57(1)	1.4(6)	2.93(5)	0.010				2–8.5	1.3–3.1
450	5.0(7)	2.56(2)	1.4(6)*	2.90(5)	0.010				2–8	1.3–3.1
Sol9										
T	n_O	r_O (Å)	n_{Cl}	r_{Cl} (Å)	σ (Å^2)	E0 (eV)	χ^2_{red}	r-factor	k-range (Å^{-1})	R-range (Å)
30	8.5(6)	2.58(1)			0.006(2)	10.1(4)	101	0.018	2–8	1.3–4
200	7.3(6)	2.58(1)	1.0 (fix)	2.98(5)	0.009				2–8	1.3–3.2
300	6.2(8)	2.58(2)	1.5(9)	2.93(5)	0.010				2–8	1.4–3.2
400	5.1(8)	2.58(2)	2.2(9)	2.91(4)	0.011				2–8	1.4–3.2
450	4.5(7)	2.59(2)	2.5(9)	2.90(3)	0.012				2–7.8	1.4–3.2
500	3.5(5)	2.59(3)	3.5(9)	2.90(2)	0.012				2–7	1.4–3.2
Sol13										
T	n_O	r_O (Å)	n_{Cl}	r_{Cl} (Å)	σ (Å^2)	E0 (eV)	χ^2_{red}	r-factor	k-range (Å^{-1})	R-range (Å)
30	9.3(7)	2.58(1)			0.008(1)	9.5(5)	70	0.016	2–8.2	1.3–3
200	8.8(8)	2.59(1)			0.011				2–8.2	1.3–3
300	7.8(7)	2.57(1)	1.0 (fix)	2.97(7)	0.012				2–8.2	1.3–3
400	6.1(7)	2.58(2)	1.4(7)	2.90(5)	0.014				2–8.2	1.3–3

*Constrained to be same as n_{Cl} at 400 °C.

hydrothermal fluids at temperatures > 400 °C. Given the intensive CPU requirements for *ab initio* MD simulations, we calculated the formation constants for the $LaCl_n^{3-n}$ complexes with n = 1, 2, 3), which are predominant under most hydrothermal conditions and more widely studied in the literature.

Fig. 4 shows an example of calculating the formation constants of reaction (1) via the *ab initio* integration method. The Helmholtz free energy $\Delta A_{I\to F}$ of reaction (1) was obtained by integrating the mean constrained force ($f(r)$) over La(III)-Cl distances ranging from the average equilibrium La(III)-Cl distance determined from *ab initio* MD (r_I in Fig. 4) to 6 Å (r_F in Fig. 4), where the interaction between La(III) and Cl^- is negligible. The constrained force is near zero at both initial and final distances ($f(r_I)$ = -2.6 kJ/(mol·Å)-; $f(r_F)$ = -1.2 kJ/(mol·Å)). Along the reaction path from r_I to r_F, $f(r)$ reached a minimum value of −31.1 kJ/(mol·Å) at r = 3.1 Å, and was near zero (-1.3 kJ/(mol·Å)) at r = 3.7 Å. At this distance (r = 3.7 Å) , the free energy also reached a maximum value (16.7 kJ/mol) and one water molecule substituted for the Cl^- that had been removed. $f(r)$ is positive between 3.8 Å to 4.8 Å, which represents the activation barrier of the ion exchange reaction. Above 5.3 Å, $f(r)$ was small, varying from −4.63 kJ/(mol•Å) at 5.3 Å to −3.94 kJ/(mol·Å) at 5.6 Å and 1.17 kJ/(mol·Å) at 6 Å, which reflects the negligible interactions between La(III) and Cl^-. The integration of $f(r)$ over the whole reaction path gives a free energy of −1.85 ± 6.95 kJ/mol for reaction (1). The free energy surfaces of the stepwise dissociation reactions.

$$LaCl_n^{3-n} = LaCl_{n-1}^{4-n} + Cl^-; (n = 1, 2, 3) \quad (5)$$

calculated with the same method are shown in Fig. 5 at each investigated P-T condition. Table 6 lists the calculated Gibbs free energy at experimental conditions ($\Delta_r G$), the Gibbs free energy at infinite dilution ($\Delta_r G^{\Theta,c}$), the Gibbs free energy after concentration and activity correction ($\Delta_r G^{\Theta}$); and the resulting formation constants (logK). The cumulative formation constants (logß) of La(III)-Cl complexes are presented in Table 7, together with the extrapolated values from the two thermodynamic models in Migdisov et al. (2009). In the review of Migdisov et al. (2016), the extrapolated formation constants of LREE-Cl complexes based on the UV-Visible experiments (Migdisov et al., 2019) are suggested to be limited to ∼ 350 °C; therefore, only the extrapolated data below 400 °C are listed in Table 7 to compare with the results of this study. The logß values of $LaCl^{2+}$ and $LaCl_2^+$ from MD and the literature are in good agreement at 300 °C. Both results show trends of increasing logß with increasing temperature. However, the increase in the values of logß with temperature from MD is sharper than that noted by Migdisov et al. (2016), especially for $LaCl^{2+}$: logß increases from 2.33 at 200 °C to 12.28 at 400 °C according to our MD results, *vs* 3.64 at 200 °C to 8.58 at 400 °C. The logß obtained from MD for both $LaCl^{2+}$ and $LaCl_2^+$ are smaller at 200 °C but higher at 400 °C than the values of Migdisov et al. (2016); these values were derived from experiment to 250 °C in relatively dilute solutions (≤0.16 m Cl_{tot}); the largest discrepancy (3.7) of logß between MD and the literature appears at 400 °C for the $LaCl_2^+$ complex.

Aside from the semi-empirical extrapolations of Haas et al. (1995), this study first provides estimates of the ther-

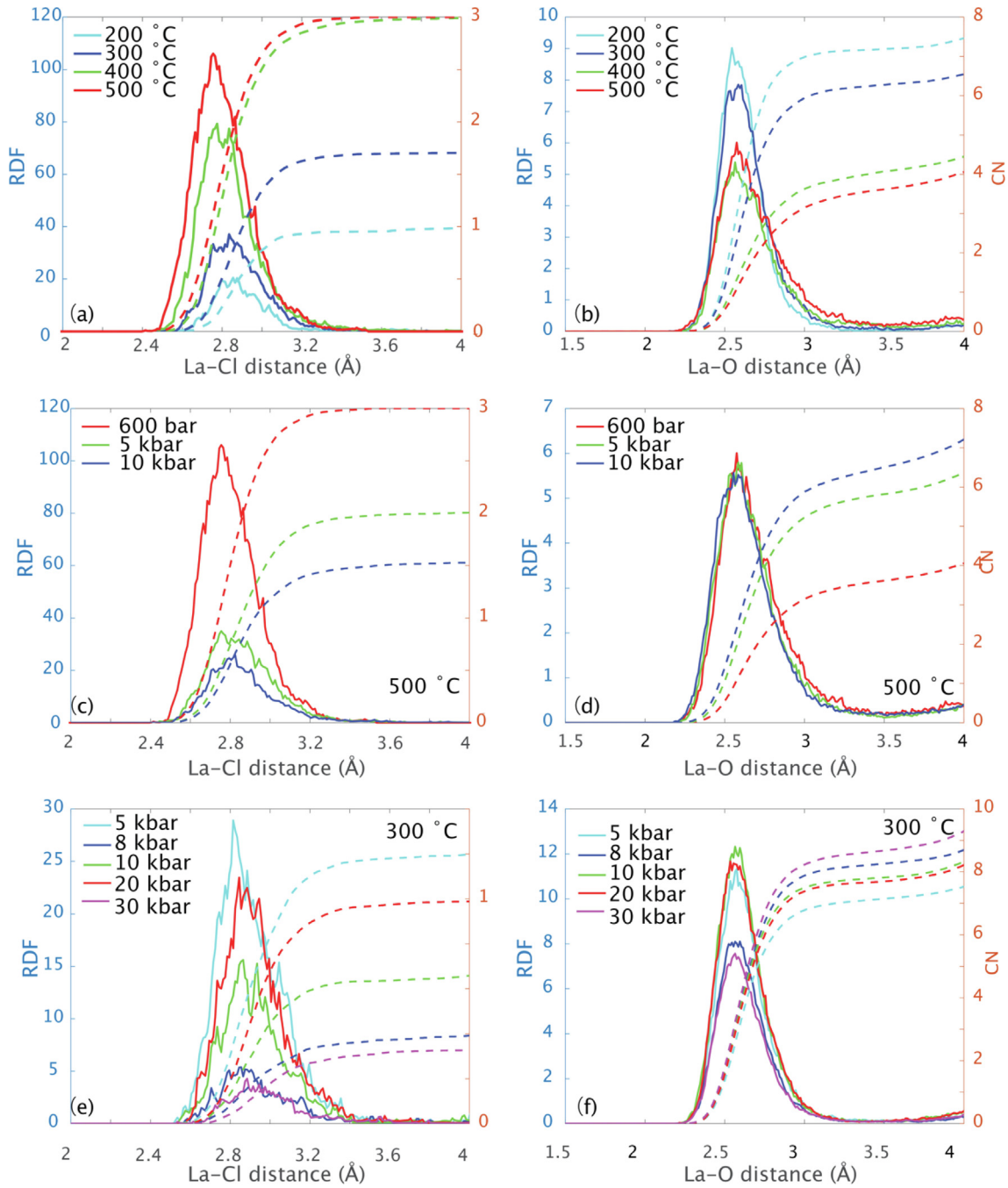

Fig. 2. Radial distribution functions of simulations in box 1. The pressures in 2(a) and 2(b) are 400 bar at 200 °C, 300 °C and 400 °C; 600 bar at 500 °C.

modynamic properties of the neutral $LaCl_3$(aq) complex from "experiments" (MD). $LaCl_3$(aq) is expected to be predominant at high temperature and low pressure conditions due to the decrease in dielectric of the water solvent (Brugger et al., 2016), an assumption confirmed by both MD and EXAFS results showing that $LaCl_3$(aq) indeed becomes an important specie in Cl-rich fluids at high temperature. Compared to the extrapolations of Haas et al. (1995), the MD results predict a higher stability of $LaCl_3$(aq) at high temperatures (≥300 °C), but are consistent within uncertainty to ~ 200 °C (Appendix 1).

In general, the energies for the stepwise introduction of a chloride in the coordination sphere of La(III) (one to three chlorides total) become more exothermic with increasing temperature, consistent with the higher stability of chloride complexes at high temperatures (Table 6). The overall trends are similar for all three chloride complexes considered in this study.

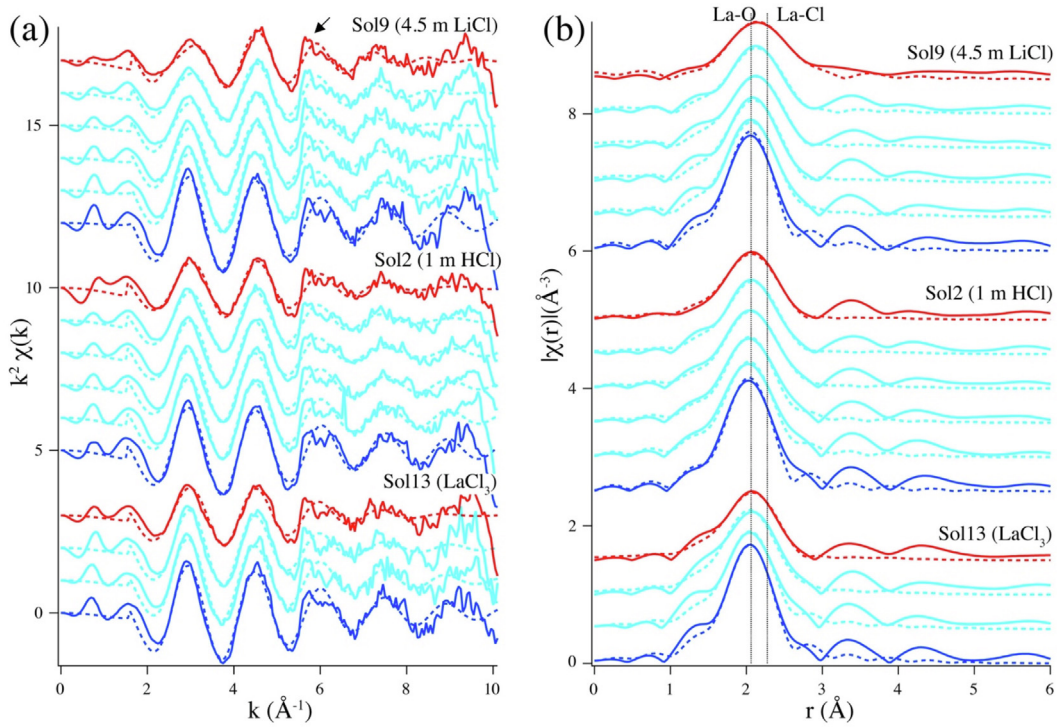

Fig. 3. EXAFS (χ (k)) and magnitude of the Fourier transform of EXAFS data (|χ (r)|) (Rehr et al., 2017). Blue = 30 °C data, red = maximum temperature (see Tables 2 and 6). The anomalously shaped peak indicated by the arrow is indicative of multi-electron excitations, however attempts to correct for this did not improve the fits.

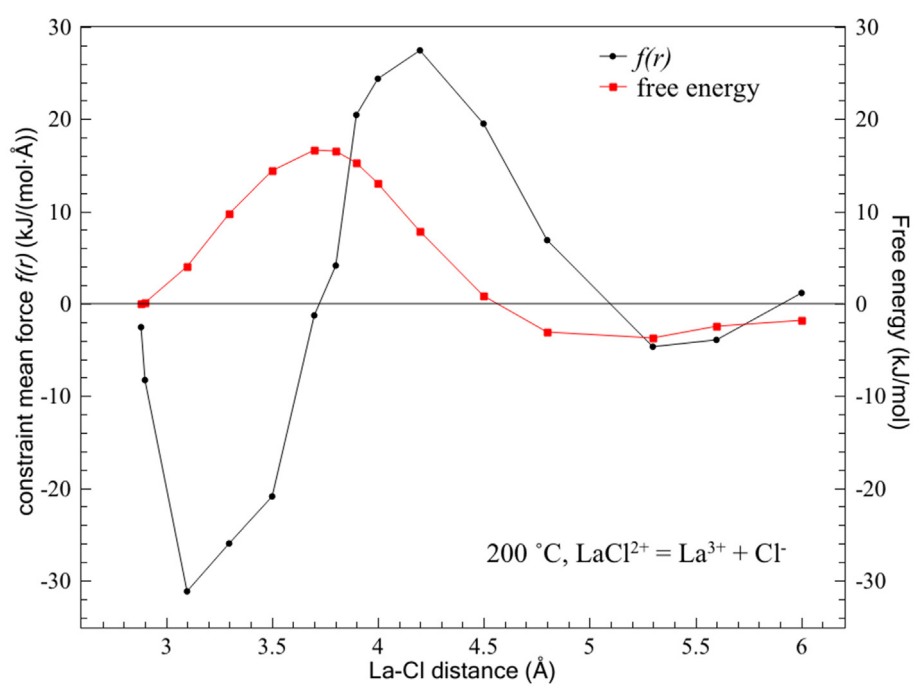

Fig. 4. Example of *ab initio* thermodynamic integrations: the constrained force (black) and the free energy surface (red) of reaction $La^{3+} + Cl^{-} = LaCl^{2+}$ at 200 °C, 400 bar.

4. DISCUSSION

4.1. Comparison of experimental and *ab-initio* MD results

The compositions of the *ab initio* MD and experimental solutions at each temperature are similar. For example, in MD box 1 the ratio of La and Cl is 1:3, comparable to Sol13 which contains 0.048 m La and a total of 0.147 m chlorine; in MD box 2 the ratio of La and Cl is 1:5, which is comparable to the high salinity solution (Sol9).

As shown in Fig. 6, there is a good agreement with the trend of decreasing total coordination number and increasing Cl coordination number with increasing temperature between MD, EXAFS (this study, and Mayanovic et al., 2009) and using the thermodynamic properties generated from solubility experiments (Migdisov et al., 2016) to calculate Cl coordination numbers from solution compositions similar to that measured by Mayanovic et al. (2009). It should be noted that the errors shown in Fig. 6 for the results derived from EXAFS fitting were calculated in quadrature, and so represent an upper bound for the actual error of the total coordination number, due to the correlation between the coordination numbers (and their errors) of oxygen and chlorine.

In terms of absolute number (rather than trends), the average bonded chloride numbers from the thermodynamic model of Migdisov et al. (2016) calculated for the conditions of Mayanovic et al. (2009) experiments, predict significantly lower values than the experimental ones. In general, the total coordination numbers listed by Mayanovic et al.

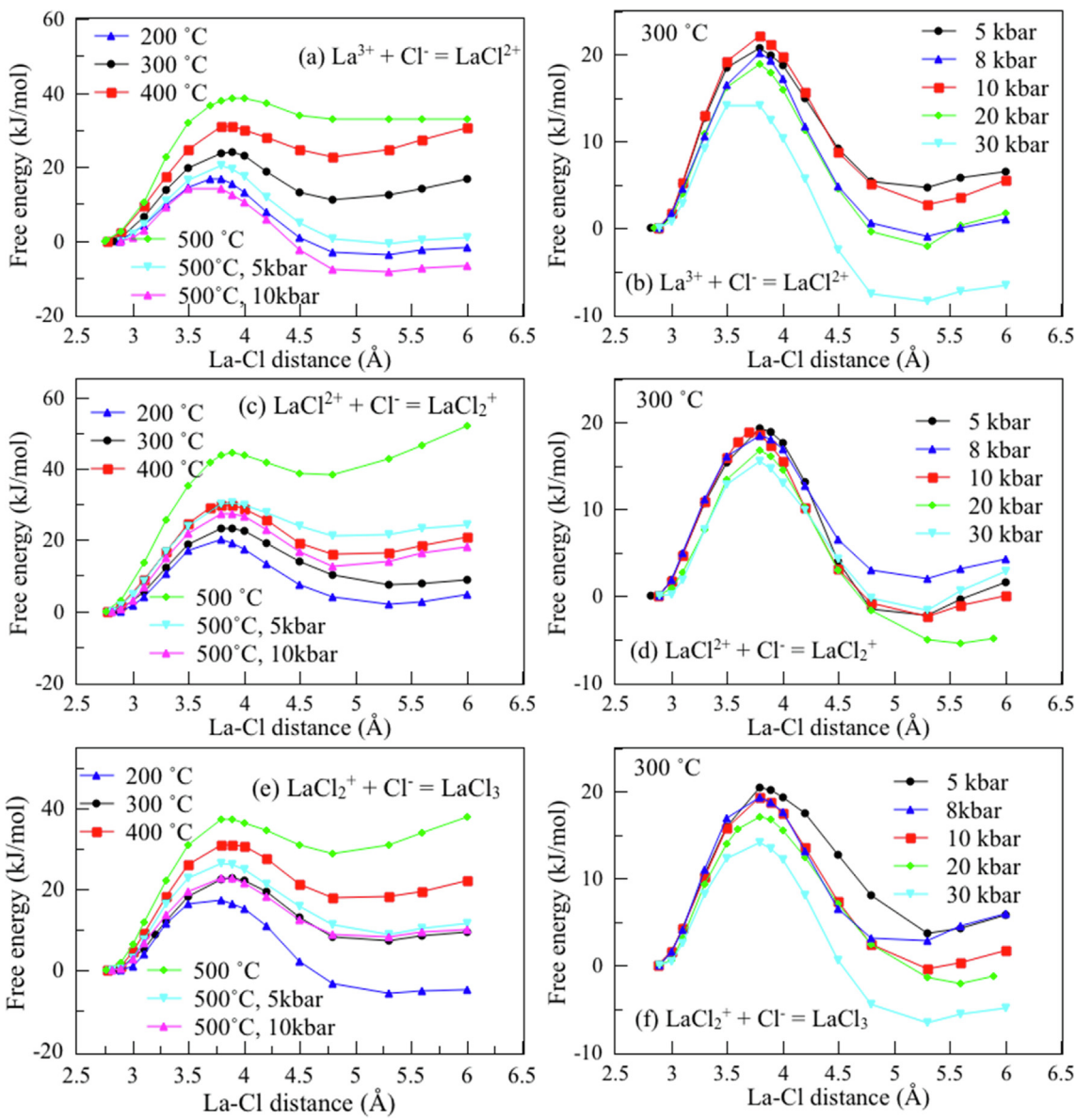

Fig. 5. Free energy surface of all calculations from thermodynamic integration in this study. In Fig. 4(a), 4(c) and 4(e), the pressures are 400 bar at 200 °C and 300 °C; 600 bar at the 500 °C which pressure was unmarked (green line).

Table 6
Results of thermodynamic integration study of the thermodynamics of La(III) chloride complexes: calculated Gibbs free energy of reaction (successive ligand addition) from MD ($\Delta_r G$, kJ/mol); Gibbs free energy of reaction at infinite dilution, calculated assuming unit activity coefficients ($\Delta_r G^{\Theta,c}$, kJ/mol); Gibbs free energy of reaction at infinite dilution calculated using activity correction ($\Delta_r G^{\Theta}$, kJ/mol); and logarithm of the stepwise formation constants (logK) derived from $\Delta_r G^{\Theta}$.

Reaction	T (°C)	P (bar)	$\Delta_r G$	$\Delta_r G^{\Theta,c}$	$\Delta_r G^{\Theta}$	logK
$La^{3+} + Cl^- = LaCl^{2+}$	200	400	1.85 ± 6.95	6.17	−9.31	1.03 ± 0.77
	300	400	−16.80 ± 7.52	−11.56	−42.99	3.92 ± 0.69
	300	5 k	−6.57 ± 7.66	−1.34	−14.73	1.34 ± 0.70
	300	8 k	−0.97 ± 7.37	4.27	−9.06	0.83 ± 0.67
	300	10 k	−5.50 ± 7.98	−0.26	−13.55	1.23 ± 0.73
	300	20 k	−1.75 ± 8.66	3.48	−9.54.	0.87 ± 0.79
	300	30 k	6.66 ± 8.47	11.89	−0.81	0.07 ± 0.77
	400	400	−30.71 ± 7.96	−24.56	−96.72	7.50 ± 0.62
	500	600	−32.83 ± 9.07	−25.77	−200.40	13.54 ± 0.61
	500	5 k	−29.03 ± 8.56	−21.97	−54.95	3.71 ± 0.58
	500	10 k	−15.26 ± 8.63	−8.20	−39.97	2.70 ± 0.58
$LaCl^{2+} + Cl^- = LaCl_2^+$	200	400	−4.63 ± 7.36	−1.90	−11.81	1.30 ± 0.81
	300	400	−8.65 ± 7.41	−5.35	−24.99	2.28 ± 0.68
	300	5 k	−1.60 ± 7.78	−1.70	−7.19	0.66 ± 0.71
	300	8 k	−4.32 ± 7.16	−1.01	−9.83	0.90 ± 0.65
	300	10 k	−0.07 ± 7.63	3.23	−5.53	0.50 ± 0.70
	300	20 k	4.97 ± 8.16	8.27	−0.21	0.02 ± 0.74
	300	30 k	−2.83 ± 7.94	0.47	−7.69	0.7 ± 0.72
	400	400	−20.92 ± 8.65	−17.04	−61.60	4.78 ± 0.67
	500	600	−51.88 ± 9.15	−47.42	−157.36	10.63 ± 0.62
	500	5 k	−24.25 ± 8.2	−19.80	−40.88	2.76 ± 0.55
	500	10 k	−17.99 ± 8.66	−13.54	−33.80	2.28 ± 0.58
$LaCl_2^+ + Cl^- = LaCl_3$	200	400	4.74 ± 6.87	4.74	0.51	−0.06 ± 0.76
	300	400	−9.44 ± 7.27	−9.44	−17.81	1.62 ± 0.66
	300	5 k	−5.81 ± 6.88	−5.81	−9.66	0.88 ± 0.63
	300	8 k	−5.90 ± 7.59	−5.90	−9.71	0.89 ± 0.69
	300	10 k	−1.73 ± 7.99	−1.73	−5.51	0.50 ± 0.73
	300	20 k	1.31 ± 8.11	1.31	−2.32	0.21 ± 0.74
	300	30 k	4.98 ± 7.49	4.98	1.52	−0.14 ± 0.68
	400	400	−22.22 ± 8.64	−22.22	−41.26	3.20 ± 0.67
	500	600	−37.89 ± 8.70	−33.89	−85.76	5.80 ± 0.59
	500	5 k	−11.61 ± 8.53	−11.61	−20.71	1.40 ± 0.58
	500	10 k	−10.17 ± 8.58	−10.17	−13.98	1.27 ± 0.78

(2009) are high (e.g, 10.5 for the aqua ion). The values predicted from the thermodynamic model overlap with the chloride numbers fitted for our two chloride-poor solutions (Sol2 and Sol13; Fig. 6), but are lower than the values from the MD runs. In contrast, chloride numbers predicted by MD and those derived from the fitting of the EXAFS data of the high salinity solution (Sol9) overlap within experimental uncertainty. We note that at low temperature, ligand exchange reactions of chloride are slow due to the slow kinetics; i.e., the species determined by *ab initio* MD could be metastable as the time range of the simulation is much shorter than the ligand residence time. This could lead to an overestimation by the *ab initio* MD results, which is particularly noticeable of for the simulation of box 2 at 200 °C.

In general, the La(III)-O bond lengths determined from EXAFS were consistent with the *ab initio* MD results in this study, 2.57(1)–2.59(2) Å from experiments at 200–400 °C and 400 bar compared to 2.55–2.62 Å from MD. The experimentally derived La(III)-Cl bond lengths under the same conditions (2.90(5)–3.02(20) Å) tend to be longer than those from MD (2.73 – 2.91 Å). Both MD and experiments show a decrease of La(III)-Cl distances with increasing temperature, but the MD results show a sharper decrease of 0.16 Å (job 3a and job 3c). It should be noted however, that (i) the lower temperature EXAFS La(III)-Cl bond lengths have large errors (i.e. where very little Cl is present), and (ii) the multi-methods study of aqueous La(III)-Cl complexes at room temperature by Díaz-Moreno et al. (2011) (Table 1) also reveals shorter La(III)-Cl bond lengths compared to EXAFS measurements.

4.2. Extrapolation of thermodynamic properties

To quantify the transport of an element under hydrothermal conditions, thermodynamic properties of all relevant aqueous species need to be known over a wide range of pressures and temperatures. This is usually achieved by using semi-empirical equations of states (EOS) to extrapolate the limited conditions covered by

Table 7
Cumulative formation constants (logß) of the La(III)-Cl^- complexes derived from MD simulations (thermodynamic integration) in this study, compared to and the extrapolations of logß of La(III)-Cl^- species to 400 °C using HKF parameters from Migdisov et al. (2009).

reaction	T (°C)	P (bar)	logß	Previous studies	T (°C)	P (bar)	logß
$La^{3+} + Cl^- = LaCl^{2+}$	200	400	1.03 ± 0.77	2.29[a], 2.37[b]	300	5 k	1.34 ± 0.70
	300	400	3.92 ± 0.69	4.31[a], 3.69[b]	300	8 k	0.83 ± 0.67
	400	400	7.50 ± 0.62	7.07[a], 5.29[b]	300	10 k	1.23 ± 0.73
	500	600	13.54 ± 0.61		300	20 k	0.87 ± 0.79
	500	5 k	3.71 ± 0.58		300	30 k	0.07 ± 0.77
	500	10 k	2.70 ± 0.58				
$La^{3+} + 2Cl^- = LaCl_2^+$	200	400	2.33 ± 1.12	3.64[c]	300	5 k	2.00 ± 1.00
	300	400	6.20 ± 0.97	5.98[c]	300	8 k	1.73 ± 0.93
	400	400	12.28 ± 0.91	8.58[c]	300	10 k	1.73 ± 1.01
	500	600	24.17 ± 0.87		300	20 k	0.89 ± 1.08
	500	5 k	6.47 ± 0.80		300	30 k	0.77 ± 1.05
	500	10 k	4.98 ± 0.82				
$La^{3+} + 3Cl^- = LaCl_3^+$	200	400	2.26 ± 1.35		300	5 k	2.88 ± 1.18
	300	400	7.82 ± 1.17		300	8 k	2.62 ± 1.15
	400	400	15.48 ± 1.13		300	10 k	2.23 ± 1.24
	500	600	29.97 ± 1.05		300	20 k	1.10 ± 1.31
	500	5 k	7.87 ± 0.99		300	30 k	0.56 ± 1.20
	500	10 k	6.25 ± 1.13				

Notes: Migdisov et al. (2009) give two different HKF fits for $LaCl^{2+}$; (a) cumulative formation constants using properties from their Table 5; (b) from their Table 7. (c) Cumulative formation constants for $LaCl_2^+$ based on properties listed in Table 6 in Migdisov et al. (2009).

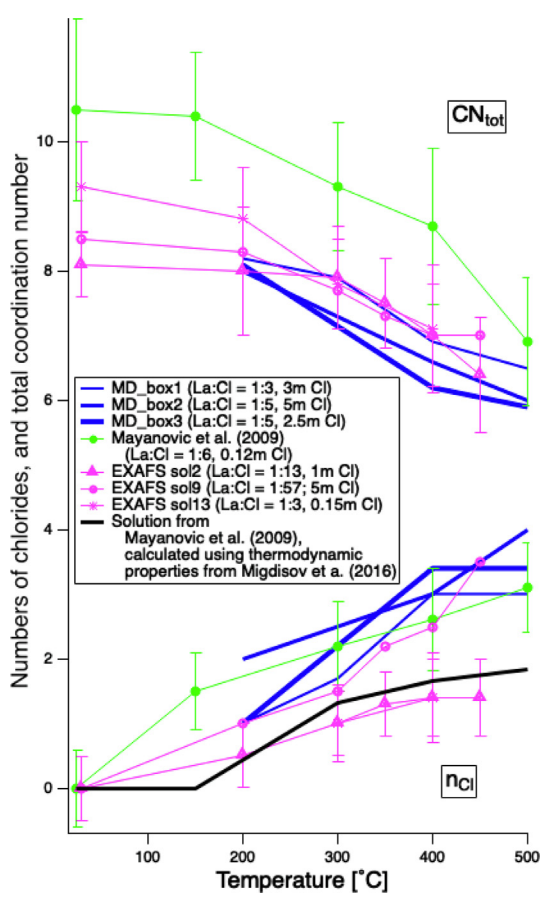

Fig. 6. Summary of the temperature dependence of the chloride complexing and total coordination number (CN_{tot}) from this study (data in Tables 4 and 5) and from the literature.

experiments. The most widely used EOS in hydrothermal geochemistry is the HKF model of Helgeson et al. (1981), revised by Tanger and Helgeson (1988). HKF relies on semi-empirical correlations with the dielectric constant and density of water, and the P-T dependence of the molar volume of each species (i) is described by five empirical parameters (Born coefficient ω^i and a_1^i to a_4^i); the heat capacity (Cp) is modelled using another two empirical parameters (c_1 and c_2) as $f(T, c_1, c_2, \omega)$ (Shock and Helgeson, 1988). The HKF model is applicable to pressures of 5 kbar and temperature of 1000 °C, limits imposed by the lack of the key properties of water (dielectric constant) at the time. Sverjensky et al. (2014) combined new measurements of the dielectric constants (Pan et al., 2013) and densities (Zhang and Duan, 2005) of water to high P, T (60 kbar, 1200 °C) into a revised HKF model named Deep Earth Water model (DEW), enabling modelling of fluid-rock interaction to 1200 °C, 60 kbar (Zhong et al. 2020).

Here, we fit a new set of DEW-HKF parameters for La (III)-Cl species to the Gibbs free energy of formation from the elements ($\Delta_f G^0(25\ \mathring{C}, 1\ bar)$) calculated from our MD-derived formation constants, combined with the experimental P_{sat} data at 150, 200, and 250 °C from Migdisov et al. (2009), and the well-constrained room temperature properties of $LaCl^{2+}$ and $LaCl_2^+$ selected by Migdisov et al. (2016). The room temperature Gibbs free energy of formation from the elements ($\Delta_f G^0(25\ \mathring{C}, 1\ bar)$) for $LaCl_3$(aq) was estimated from $LaCl^{2+}$ and $LaCl_2^+$ by assuming a linear trend of $\Delta_f G^0(25\ \mathring{C}, 1\ bar)$ of $LaCl_n^{3-n}$ complexes from n = 1 to 3, as observed from example in the properties listed by Haas et al. (1995) (Appendix 1). Finally, the MD data at 200 °C, 400 bar; 300 °C at all pressures; 500 °C, 5 kbar

Table 8
DEW-HKF equation of state parameters for aqueous La(III)-Cl species.

	$LaCl^{2+}$	$LaCl_2^+$	$LaCl_3(aq)$
$\Delta_f G^0(25\ ^\circ C, 1bar)$, $cal\ mol^{-1}$	−196214	−227685	−258659
$S^0(25^\circ C, 1bar)$, $cal\ mol^{-1}K^{-1}$	−20.419	−6.385	−7.501
$c_p^0(25^\circ C, 1bar)$, $cal\ mol^{-1}K^{-1}$	−40.0	4.1	60.5
$V^0(25^\circ C, 1bar)$, $cm^3 mol^{-1}$	−20.6	11.2	27.2
$a1*10$, $cal\ mol^{-1}\ bar^{-1}$	−0.5840	3.4669	6.7855
$a2*10^{-2}$, $cal\ mol^{-1}$	−9.2412	0.9351	2.1774
$a3$, $cal\ K\ mol^{-1}\ bar^{-1}$	9.3726	5.4540	3.0124
$a4*10^{-4}$, $cal\ mol^{-1}\ K$	−2.3970	−2.8177	−2.8690
$c1$, $cal\ mol^{-1}\ K^{-1}$	−4.6961	14.5430	41.2445
$c2*10^{-4}$, $cal\ mol^{-1}\ K$	−11.1879	−2.1994	9.2793
$\omega * 10^{-5}$, $cal\ mol^{-1}$	1.3671	0.6484	−0.0380
Z	2	1	0

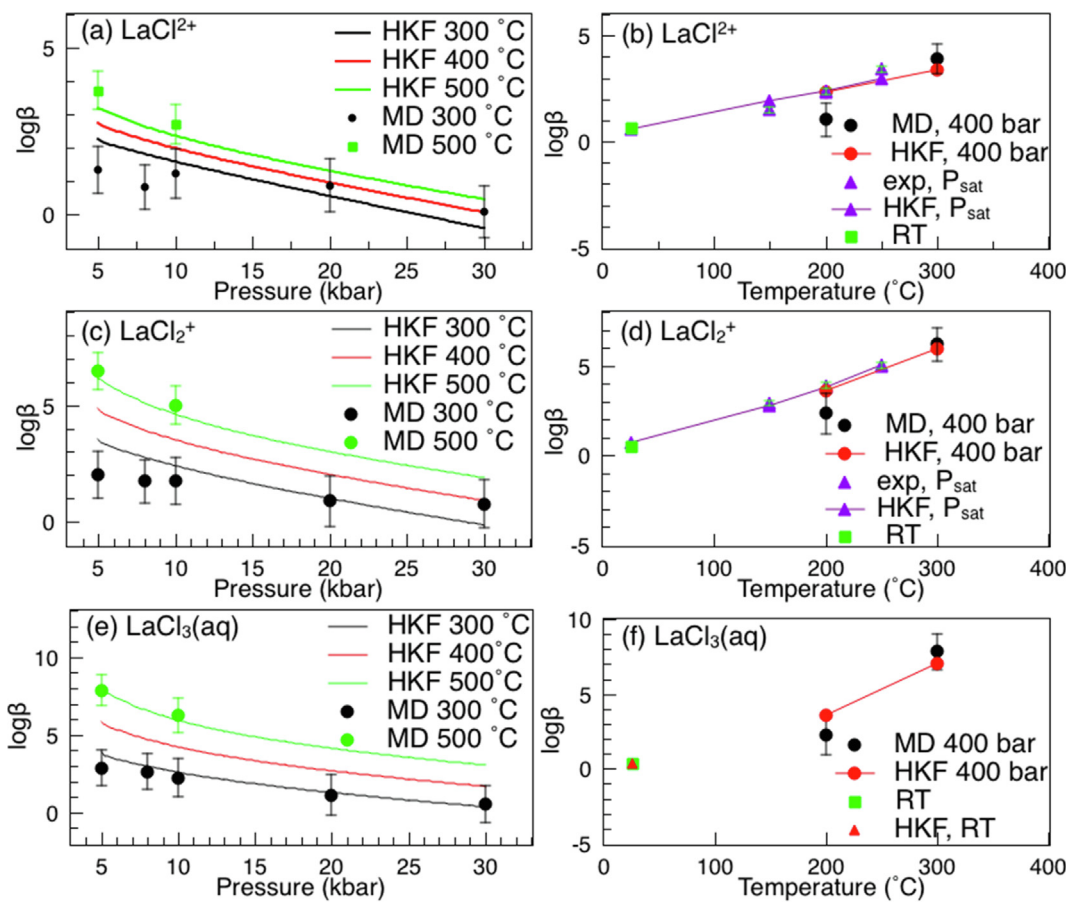

Fig. 7. The "experimental" (experiments + MD) formation constants and the fitted formation constants using the HKF parameters in Table 8 of the La-Cl species. In (b), (d) and (e), the P_{sat} points are from the experiments of Migdisov et al. (2009); the room temperature (RT) points are the properties selected by the review of Migdisov et al. (2016) for $LaCl^{2+}$ (b) and $LaCl_2^+$ (d), and those extrapolated in this study for $LaCl_3(aq)$ (see text for details). In all panels, the data points labelled 'MD' are those derived from the simulations in this study (Table 7); note that the simulations at low water density were excluded from the fits and are not shown. The lines labelled 'HKF' are the predictions using the HKF EOS parameters listed in Table 8.

and 10 kbar in Table 7 were used in the fitting. Note that the MD datapoints at 400 °C, 400 bar (density of pure water 0.52 g/cm^3) and 500 °C, 600 bar (0.34 g/cm^3) were excluded from the fitting due to the intrinsic limitations of the HKF-EOS for low density solutions (Sverjensky et al., 2014). The aim of the fitting is to provide a general model that accurately reproduces the available low T data (given the highest level of confidence), as well as the new

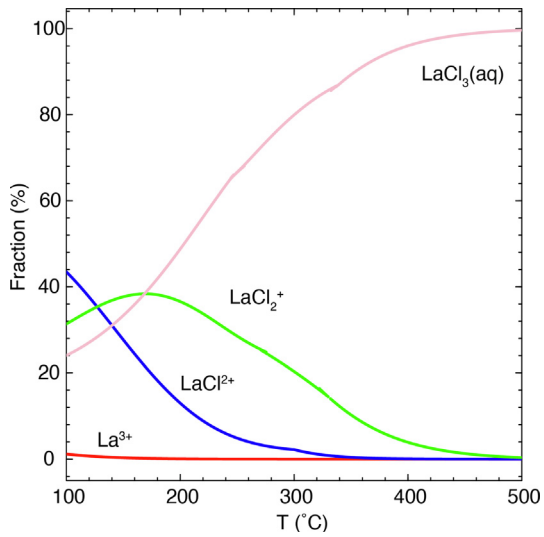

Fig. 8. Distribution of La-Cl species as a function of temperature at 1 kbar and pH = 6, modelled in 0.001 m $LaCl_3$ + 5 m NaCl solution. Note that La-hydroxide complexes are excluded because of poor reliability (Migdisov et al. 2016); they would be important at pH = 6, but negligeable at pH_T = 3.

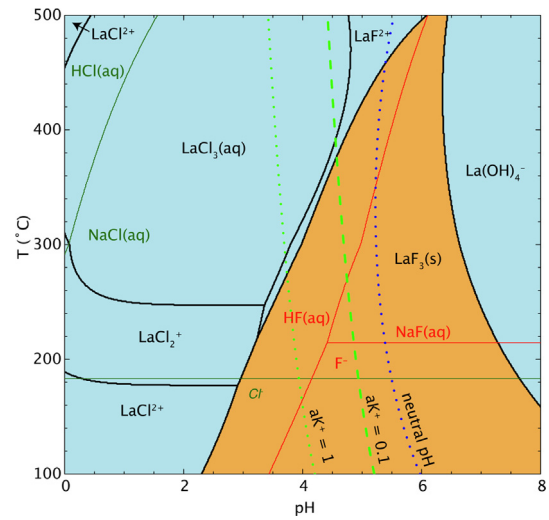

Fig. 10. Predominant aqueous La species and mineral stability boundaries as a function of pH and temperature at 1 kbar in a sodic brine containing a total amount of 5 m chlorine, 0.01 m fluorine and 1 ppb La. The red solid line shows the iso-activity boundaries among predominant aqueous species of fluorine (F^-, HF(aq), and NaF(aq)), and the green solid lines among chlorine species (HCl(aq) and NaCl(aq)). The bold green dotted line shows the KMQ (K-feldspar-muscovite-quartz) buffer at $aK^+ = 1$; the green dashed line is at $aK^+ = 0.1$, the blue dotted line is neutral pH.

constraints at elevated T and salinities from the new MD and EXAFS results.

The Gibbs free energies of formation from the elements of each aqueous species ($\Delta_f G^0_{LaCl_n^{3-n}}$, n = 1–3) at different P-T were calculated from the ligand addition reactions using the logß listed in Table 7 and Gibbs free energies of formation from the elements of La^{3+} and Cl^- from Shock & Helgeson (1988). The equation of state of water of Zhang and Duan (2005) was selected to calculate the density of water in the DEW calculations. We fitted $\Delta_f G^0(25\ ^\circ C, 1bar)$, molar entropy $\bar{S}^0(25\ ^\circ C, 1bar)$, partial molar volume ($\bar{V}^0(25\ ^\circ C, 1bar)$), and molar heat capacity ($\bar{c}_p^{\,0}(25\ ^\circ C, 1bar)$) using correlations for the $a_1 - a_4$, $c_1 - c_2$, and ω parameters from Sverjensky et al. (2014). The fit was performed by minimizing the sum of the square of the difference between predicted $\Delta_f G^p_{LaCl_n^{3-n}}$ and 'experimental' $\Delta_f G^0_{LaCl_n^{3-n}}$ (n = 1–3), weighted by the experimental errors of each data point. The final recommended DEWHKF parameters are listed in Table 8. The formation constants of La(III)-Cl species predicted using these HKF parameters are compared in Fig. 7 to the experimental values includes this study and previous studies that were used in the fitting; values calculated using different models are listed in Appen-

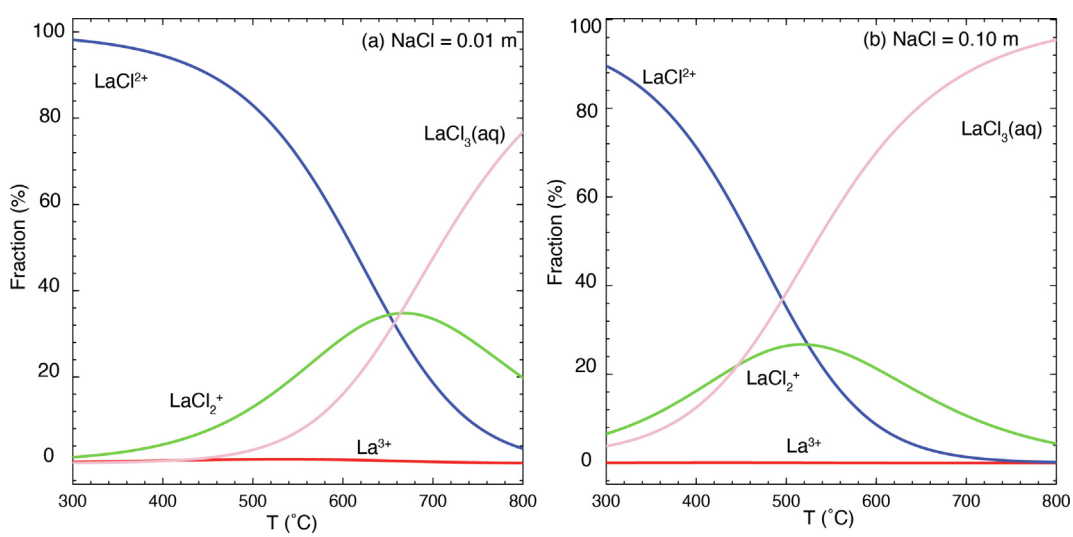

Fig. 9. Distribution of La-Cl species as a function of temperature at 45 kbar and pH = 6, modelled in 0.001 m $LaCl_3$ + (a) 0.01 m and (b) 0.1 m NaCl solutions.

dix 1 together with previous HKF EOS parameters from Migdisov et al. (2009) and Haas et al., (1995).

5. CONCLUSION: LA IN CRUSTAL FLUIDS

We employed the CHNOSZ program (Dick, 2019) to model the distribution of La(III)-Cl complexes at elevated temperatures, typical upper crustal and subduction pressure (Figs. 8 and 9) and the speciation of La in hydrothermal fluids (Fig. 10). Thermodynamic data of LaF^{2+} and LaF_3(s) were taken from Migdisov et al. (2009), La^{3+} from Shock and Helgeson (1988), and the other aqueous species are sourced from CHNOSZ's default OBIGT database, which includes the aqueous species from Sverjensky et al. (1997).

Fig. 8 presents the distribution of La(III)-Cl species as a function of temperature at 1 kbar in Cl-only solutions (5 m Cl_{tot}; pH = 6). It illustrates how many Cl^- will bond with La (III) with increasing temperature. At 100 °C the solution contains mainly $LaCl_2^+$ and $LaCl^{2+}$. As the temperature increases to ~160 °C, $LaCl_2^+$ dominants but the fraction of $LaCl_2^+$ and $LaCl^{2+}$ decrease while the fraction of $LaCl_3$(aq) increases. At temperatures between 160 °C and 500 °C, the percentage of $LaCl_3$(aq) keeps increasing, and above ~400 °C, $LaCl_3$(aq) is the only species existing in significant amounts in the solution. The trends of the distribution of La(III)-Cl species are consistent with our experimental data at temperature over 300 °C. The predominance of the high order $LaCl_3$(aq) complex in brines is supported by the EXAFS results (Sol9, Table 5); at 500 °C the EXAFS show 3.5(9) chloride in the first shell, and at 400 °C 2.2(9), still consistent with a predominance of $LaCl_3$(aq) within uncertainty. Under pressures characteristic of subduction zones (4.5 GPa) fluids, $LaCl^{2+}$ is predominant in low salinity fluids from 300 °C to ~650 °C (Fig. 9a). Over this temperature range, the fraction of $LaCl^{2+}$ decreases while the fractions of $LaCl_2^+$ and $LaCl_3$(aq) increases. Above 650 °C, the fractions of $LaCl^{2+}$ and $LaCl_2^+$ decrease as they are replaced by $LaCl_3$(aq). At 800 °C, $LaCl_3$(aq) is dominant in the fluids. For fluids containing higher concentrations of NaCl (Fig. 9b, NaCl = 0.1 m), the trends of the fraction of the species are similar to Fig. 9a, but $LaCl_3$(aq) becomes predominant at temperatures as low as 500 °C. In their MD study of the Y(III)-Cl speciation at 800 °C, 4.5 GPa, Stefanski and Jahn (2020) predicted that Y(III) exists as the Y^{3+} aqua ion in highly dilute fluids (NaCl < 0.001 m), and about half YCl^{2+} and Y^{3+} at a NaCl concentration of 0.01 m. LREE tends to form higher order of Cl species than HREE, thus are expected to be more mobile than HREE in subduction-zone fluids. The hydroxide complexes maybe significant at this condition ($pH_T = 6$), but would be negligeable at $pH_T = 3$, however, due to the limited available data of REE-hydrolysis (Migdisov et al., 2016), the La(III) hydroxide complexes are not considered in this model.

Fig. 10 shows the solubility of LaF_3(s) (as proxy for La-minerals) and the predominant aqueous La(III) species as a function of pH and temperature at 1 kbar in a Cl-rich brine (5 m Cl). LaF_3(s) solubility is minimum at low temperature and near-neutral pH (Fig. 10). At the conditions selected for this diagram (brine with 5 m total chlorine, and 0.01 m fluorine, i.e. a Cl:F ratio of 500, typical of basement, magmatic, and metamorphic fluids (Xing et al. 2019), fluoride complexes are predicted to play a minor role at medium temperatures (250 – 350 °C) at pH buffered by K-feldspar-muscovite-quartz (KMQ). At most other acidic conditions, La(III)-Cl complexes predominate in solution, which shows that Cl^- is an effective ligand for La transport. As hydrofluoric acid associates strongly at high temperature, the activity of the free fluoride ion become very low (Migdisov et al., 2019; Xing et al., 2019), which favours La(III)-Cl complexes; the high order $LaCl_3$(aq) complex was dominant over a wide pH range above 300 °C. The stability of the high order $LaCl_3$(aq) complex at elevated temperature is important for explaining the transport of LREE in magmatic hydrothermal brines, and suggests that mixing of brines and low-salinity fluids, especially coupled with cooling, provides an efficient mechanism for REE precipitation.

DECLARATION OF COMPETING INTEREST

The authors declare that they have no known competing financial interests or personal relationships that could have appeared to influence the work reported in this paper.

ACKNOWLEDGEMENTS

We thank Dimitri Sverjensky and an anonymous reviewer for providing insightful reviews, and Associate Editor Zoltan Zajacz for handling the manuscript. This research is supported by Australian Research Council Discovery grant DP190100216 to JB; a Monash University post-graduate publication award to Q.G.; CSIRO Deep Earth Imaging Future Science Platform (YM); and EU Horizon2020 Marie Curie Individual Fellowship 797145 to ML. The MD simulation of this work was supported by resources provided by the Pawsey Supercomputing Centre with funding from the Australian Government and the Government of Western Australia, the National Computational Infrastructure (NCI) supported by the Australian Government, and the high-performance computers in CSIRO. We are grateful to the European Synchrotron Research Facility (Grenoble, France) for providing beamtime, and to the Australian International Synchrotron Access Program (ISAP) managed by the Australian Synchrotron, part of ANSTO, and funded by the Australian Government, for travel funding.

APPENDIX A. SUPPLEMENTARY MATERIAL

Supplementary material to this article can be found online at https://doi.org/10.1016/j.gca.2022.02.032.

REFERENCES

Australian critical minerals prospectus (2020) Australia Government. https://www.austrade.gov.au/ArticleDocuments/5572/Australian_Critical_Minerals_Prospectus.pdf.aspx.

Allen M. and Tildesley D. (1987) *Computer Simulation of Liquids*. Oxford Univ. Press, Oxford.

Allen P. G., Bucher J. J., Shuh D. K., Edelstein N. M. and Craig I. (2000) Coordination chemistry of trivalent lanthanide and actinide ions in dilute and concentrated chloride solutions. *Inorg. Chem.* **39**, 595–601.

Anderson A. J., Jayanetti S., Mayanovic R. A., Bassett W. A. and Chou I.-M. (2002) X-ray spectroscopic investigations of fluids in the hydrothermal diamond anvil cell: the hydration structure of aqueous La^{3+} up to 300 °C and 1600 bars. *Am. Mineral.* **87**, 262–278.

Bankura A., Carnevale V. and Klein M. L. (2014) Hydration structure of Na^+ and K^+ from *ab initio* molecular dynamics based on modern density functional theory. *Mol. Phys.* **112**, 1448–1456.

Becke A. D. (1988) Density-functional exchange-energy approximation with correct asymptotic behavior. *Phys. Rev. A* **38**, 3098–3100.

Beuchat C., Hagberg D., Spezia R. and Gagliardi L. (2010) Hydration of lanthanide chloride salts: a quantum chemical and classical molecular dynamics simulation study. *J. Phys. Chem. B* **114**, 15590–15597.

Brugger J., Etschmann B., Liu W., Testemale D., Hazemann J. L., Emerich H., van Beek W. and Proux O. (2007) An XAS study of the structure and thermodynamics of Cu(I) chloride complexes in brines up to high temperature (400°C, 600bar). *Geochim. Cosmochim. Acta* **71**, 4920–4941.

Brugger J., Etschmann B., Pownceby M., Liu W., Grundler P. and Brewe D. (2008) Oxidation state of europium in scheelite: tracking fluid–rock interaction in gold deposits. *Chem. Geol.* **257**, 26–33.

Brugger J., Liu W., Etschmann B., Mei Y., Sherman D. M. and Testemale D. (2016) A review of the coordination chemistry of hydrothermal systems, or do coordination changes make ore deposits? *Chem. Geol.* **447**, 219–253.

Bruyère R., Prat A., Goujon C. and Hazemann J.-L. (2008) A new pressure regulation device using high pressure isolation valves. *J. Phys.: Conf. Ser. IOP Publishing* 122003.

Bühl M., Sieffert N., Partouche A., Chaumont A. and Wipff G. (2012) Speciation of La(III) chloride complexes in water and acetonitrile: a density functional study. *Inorg. Chem.* **51**, 13396–13407.

Campbell L., Rehr J. J., Schenter G. K., McCarthy M. I. and Dixon D. (1999) XAFS Debye-Waller factors in aqueous Cr+3 from molecular dynamics. *J. Synchrotron Radiat.* **6**, 310–312.

Car R. and Parrinello M. (1985) Unified approach for molecular dynamics and density-functional theory. *Phys. Rev. Lett.* **55**, 2471–2474.

Chantler C. T. (1995) Theoretical form factor, attenuation, and scattering tabulation for Z= 1–92 from E= 1–10 eV to E= 0.4–1.0 MeV. *J. Phys. Chem. Ref. Data* **24**, 71–643.

Clavaguéra C., Pollet R., Soudan J. M., Brenner V. and Dognon J. P. (2005) Molecular dynamics study of the hydration of lanthanum(III) and europium(III) including many-body effects. *J. Phys. Chem. B* **109**, 7614–7616.

Cossy C., Helm L. and Merbach A. E. (1989) High-pressure NMR study. 38. Water-exchange mechanisms on the terbium to thulium octaaqualanthanide(III) ions: a variable-pressure oxygen-17 NMR study. *Inorg. Chem.* **28**, 2699–2703.

D'Angelo P., De Panfilis S., Filipponi A. and Persson I. (2008) High-energy X-ray absorption spectroscopy: a new tool for structural investigations of lanthanoids and third-row transition elements. *Chem. –Eur. J.* **14**, 3045–3055.

D'Angelo P., Migliorati V. and Guidoni L. (2010) Hydration properties of the bromide aqua ion: the interplay of *First Principle* and classical molecular dynamics, and X-ray absorption spectroscopy. *Inorg. Chem.* **49**, 4224–4231.

D'Angelo P. and Spezia R. (2012) Hydration of lanthanoids(III) and actinoids(III): an experimental/theoretical saga. *Chem. –Eur. J.* **18**, 11162–11178.

Díaz-Moreno S., Ramos S. and Bowron D. T. (2011) Solvation structure and ion complexation of La 3+ in a 1 molal aqueous solution of lanthanum chloride. *J. Phys. Chem. A* **115**, 6575–6581.

Dick J. M. (2019) CHNOSZ: thermodynamic calculations and diagrams for geochemistry. *Front. Earth Sci.* **7**, 180.

Driesner T. (2007) The system H_2O–NaCl. Part II: Correlations for molar volume, enthalpy, and isobaric heat capacity from 0 to 1000°C, 1 to 5000bar, and 0 to 1 XNaCl. *Geochim. Cosmochim. Acta* **71**, 4902–4919.

Driesner T. and Heinrich C. A. (2007) The system H2O–NaCl. Part I: Correlation formulae for phase relations in temperature–pressure–composition space from 0 to 1000°C, 0 to 5000bar, and 0 to 1 XNaCl. *Geochim. Cosmochim. Acta* **71**, 4880–4901.

Etschmann B. E., Liu W., Testemale D., Müller H., Rae N. A., Proux O., Hazemann J. L. and Brugger J. (2010) An *in situ* XAS study of copper(I) transport as hydrosulfide complexes in hydrothermal solutions (25–592°C, 180–600bar): Speciation and solubility in vapor and liquid phases. *Geochim. Cosmochim. Acta* **74**, 4723–4739.

Fortier S. M., Nassar N. T., Lederer G. W., Brainard J., Gambogi J., and McCullough E. A. (2018) Draft critical mineral list—summary of methodology and background information—US Geological Survey technical input document in response to Secretarial Order No. 3359 (No. 2018-1021). US Geological Survey.

Gammos C. H., Wood S. A. and Li Y. (2002) Complexation of the rare earth elements with aqueous chloride at 200° and 300℃ and saturated water vapor pressure. *Geochem. Soc Spec. Publ* **7**, 191–207.

Guan Q., Mei Y., Etschmann B., Testemale D., Louvel M. and Brugger J. (2020) Yttrium complexation and hydration in chloride-rich hydrothermal fluids: a combined ab initio molecular dynamics and *in situ* X-ray absorption spectroscopy study. *Geochim. Cosmochim. Acta* **281**, 168–189.

González-Álvarez I., Stoppa F., Yang X. Y. and Porwal A. (2021) Introduction to the special Issue, insights on carbonatites and their mineral exploration approach: a challenge towards resourcing critical metals. *Ore Geol. Rev.* **133** 104073.

Haas J. R., Shock E. L. and Sassani D. C. (1995) Rare earth elements in hydrothermal systems: estimates of standard partial molal thermodynamic properties of aqueous complexes of the rare earth elements at high pressures and temperatures. *Geochim. Cosmochim. Acta* **59**, 4329–4350.

Habenschuss A. and Spedding F. H. (1979) The coordination (hydration) of rare earth ions in aqueous chloride solutions from x-ray diffraction. II. $LaCl_3$, $PrCl_3$, and $NdCl_3$a). *J. Chem. Phys.* **70**, 3758–3763.

Hatayama H. and Tahara K. (2015) Criticality assessment of metals for Japan's resource strategy. *Mater. Trans.* **56**(2), 229–235.

Helgeson H. C., Kirkham D. H. and Flowers G. C. (1981) Theoretical prediction of the thermodynamic behavior of aqueous electrolytes by high pressures and temperatures; IV, Calculation of activity coefficients, osmotic coefficients, and apparent molal and standard and relative partial molal properties to 600 degrees C and 5kb. *Am. J. Sci.* **281**, 1249–1516.

Helm L. and Merbach A. E. (1999) Water exchange on metal ions: experiments and simulations. *Coord. Chem. Rev.* **187**, 151–181.

Helm L. and Merbach A. E. (2002) Applications of advanced experimental techniques: high pressure NMR and computer simulations. Based on the presentation given at Dalton Discussion No. 4, 10–13th January 2002, Kloster Banz, Germany. *J. Chem. Soc., Dalton Trans.*, 633–641.

Hölsä J., Lastusaari M. and Valkonen J. (1997) X-ray powder diffraction study of the stability of solid solutions in LaO (Cl1 − xBrx). *J. Alloy. Compd.* **262**, 299–304.

Humphrey W., Dalke A. and Schulten K. (1996) VMD: visual molecular dynamics. *J. Mol. Graph.* **14**, 33–38.

Ikeda T., Hirata M. and Kimura T. (2005) Hydration structure of Y3+ and La3+ compared: an application of metadynamics. *J. Chem. Phys.* **122** 244507.

Ishiguro S., Umebayashi Y. and Komiya M. (2002) Thermodynamic and structural aspects on the solvation steric effect of lanthanide(III)—dependence on the ionic size. *Coord. Chem. Rev.* **226**, 103–111.

Johansson G. and Wakita H. (1985) X-ray investigation of the coordination and complex formation of lanthanoid ions in aqueous perchlorate and selenate solutions. *Inorg. Chem.* **24**, 3047–3052.

Kleinman L. and Bylander D. M. (1982) Efficacious form for model pseudopotentials. *Phys. Rev. Lett.* **48**(20), 1425.

Kohn W. and Sham L. J. (1965) Self-consistent equations including exchange and correlation effects. *Phys. Rev.* **140**, A1133–A1138.

Lee C., Yang W. and Parr R. G. (1988) Development of the Colle-Salvetti correlation-energy formula into a functional of the electron density. *Phys. Rev. B* **37**, 785–789.

Lemmon E. W., McLinden M. O. and Friend D. G. (2000) *Thermophysical properties of fluid systems*. National Institute of Standards and Technology, Gaithersberg.

Lin I.-C., Seitsonen A. P., Coutinho-Neto M. D., Tavernelli I. and Rothlisberger U. (2009) Importance of van der Waals interactions in liquid water. *J. Phys. Chem. B* **113**, 1127–1131.

Ling M.-X., Liu Y.-L., Williams I. S., Teng F.-Z., Yang X.-Y., Ding X., Wei G.-J., Xie L.-H., Deng W.-F. and Sun W.-D. (2013) Formation of the world's largest REE deposit through protracted fluxing of carbonatite by subduction-derived fluids. *Sci. Rep.* **3**, 1776.

Liu W., Borg S. J., Testemale D., Etschmann B., Hazemann J.-L. and Brugger J. (2011) Speciation and thermodynamic properties for cobalt chloride complexes in hydrothermal fluids at 35–440 C and 600 bar: an *in situ* XAS study. *Geochim. Cosmochim. Acta* **75**, 1227–1248.

Liu X., Cheng J., Sprik M. and Lu X. (2013) Solution structures and acidity constants of molybdic acid. *J. Phys. Chem. Lett.* **4**, 2926–2930.

Louvel M., Bordage A., Tripoli B., Testemale D., Hazemann J.-L. and Mavrogenes J. (2017) Effect of S on the aqueous and gaseous transport of Cu in porphyry and epithermal systems: constraints from *in situ* XAS measurements up to 600° C and 300 bars. *Chem. Geol.* **466**, 500–511.

Luo Y.-R. and Byrne R. H. (2001) Yttrium and rare earth element complexation by chloride ions at 25○C. *J. Solution Chem.* **9**.

Marques M. A., Cabaço M. I., Marques M. I. d. B., Gaspar A. M. and Morais C. M. d. (2001) Local order in aqueous solutions of lanthanum chloride and bromide by x-ray diffraction, EXAFS and Raman spectroscopy. *J. Phys.: Condens. Matter* **13**, 4367–4385.

Mayanovic R. A., Anderson A. J., Bassett W. A. and Chou I.-M. (2009) Steric hindrance and the enhanced stability of light rare-earth elements in hydrothermal fluids. *Am. Mineral.* **94**, 1487–1490.

Mei Y., Sherman D. M., Liu W. and Brugger J. (2013) Ab initio molecular dynamics simulation and free energy exploration of copper(I) complexation by chloride and bisulfide in hydrothermal fluids. *Geochim. Cosmochim. Acta* **102**, 45–64.

Mei Y., Liu W., Sherman D. M. and Brugger J. (2014) Metal complexation and ion hydration in low density hydrothermal fluids: *ab initio* molecular dynamics simulation of Cu (I) and Au (I) in chloride solutions (25–1000 C, 1–5000 bar). *Geochim. Cosmochim. Acta* **131**, 196–212.

Mei Y., Sherman D. M., Liu W., Etschmann B., Testemale D. and Brugger J. (2015a) Zinc complexation in chloride-rich hydrothermal fluids (25–600 °C): a thermodynamic model derived from ab initio molecular dynamics. *Geochim. Cosmochim. Acta* **150**, 265–284.

Mei Y., Etschmann B., Liu W., Sherman D. M., Barnes S. J., Fiorentini M. L., Seward T. M., Testemale D. and Brugger J. (2015b) Palladium complexation in chloride- and bisulfide-rich fluids: insights from ab initio molecular dynamics simulations and X-ray absorption spectroscopy. *Geochim. Cosmochim. Acta* **161**, 128–145.

Mei Y., Etschmann B., Liu W., Sherman D. M., Testemale D. and Brugger J. (2016) Speciation and thermodynamic properties of zinc in sulfur-rich hydrothermal fluids: Insights from *ab initio* molecular dynamics simulations and X-ray absorption spectroscopy. *Geochim. Cosmochim. Acta* **179**, 32–52.

Mei Y., Liu W., Brugger J., Sherman D. M. and Gale J. D. (2018) The dissociation mechanism and thermodynamic properties of HCl(aq) in hydrothermal fluids (to 700 °C, 60 kbar) by ab initio molecular dynamics simulations. *Geochim. Cosmochim. Acta* **226**, 84–106.

Mei Y., Liu W., Brugger J. and Guan Q. (2020) Gold solubility in alkaline and ammonia-rich hydrothermal fluids: insights from *ab initio* molecular dynamics simulations. *Geochim. Cosmochim. Acta* **291**, 62–78.

Migdisov A. A., Williams-Jones A. E. and Wagner T. (2009) An experimental study of the solubility and speciation of the Rare Earth Elements (III) in fluoride- and chloride-bearing aqueous solutions at temperatures up to 300°C. *Geochim. Cosmochim. Acta* **73**, 7087–7109.

Migdisov A., Williams-Jones A. E., Brugger J. and Caporuscio F. A. (2016) Hydrothermal transport, deposition, and fractionation of the REE: experimental data and thermodynamic calculations. *Chem. Geol.* **439**, 13–42.

Migdisov A., Guo X., Nisbet H., Xu H. and Williams-Jones A. E. (2019) Fractionation of REE, U, and Th in natural ore-forming hydrothermal systems: thermodynamic modeling. *J. Chem. Thermodyn.* **128**, 305–319.

Näslund J., Lindqvist-Reis P., Persson I. and Sandström M. (2000) Steric effects control the structure of the solvated lanthanum (III) ion in aqueous, dimethyl sulfoxide, and N, N '-dimethylpropyleneurea solution. An EXAFS and large-angle X-ray scattering study. *Inorg. Chem.* **39**, 4006–4011.

Pan D., Spanu L., Harrison B., Sverjensky D. A. and Galli G. (2013) Dielectric properties of water under extreme conditions and transport of carbonates in the deep Earth. *Proc. Natl. Acad. Sci.* **110**, 6646–6650.

Persson I., D'Angelo P., De Panfilis S., Sandström M. and Eriksson L. (2008) Hydration of lanthanoid(III) ions in aqueous solution and crystalline hydrates studied by EXAFS spectroscopy and crystallography: the myth of the "Gadolinium Break". *Chem. –Eur. J.* **14**, 3056–3066.

Petit L., Vuilleumier R., Maldivi P. and Adamo C. (2008) Molecular dynamics study of the coordination sphere of trivalent lanthanum in a highly concentrated LiCl aqueous solution: a combined classical and ab initio approach. *J. Phys. Chem. B* **112**, 10603–10607.

Priyadarsini A., Dasari S. and Mallik B. S. (2020) Thermophysical properties and angular jump dynamics of water: a comparative DFT and DFT-dispersion-based molecular dynamics study. *J. Phys. Chem.* **A**, 11.

Powell D. H. and Merbach A. E. (1994) Water exchange on the light lanthanide aqua ions $[Pr(H_2O)_9]^{3+}$ and $[Nd(H_2O)_9]^{3+}$: a

variable temperature and magnetic field ^{17}O NMR study. *Magn. Reson. Chem.* **32**(12), 739–745.

Proux O., Biquard X., Lahera E., Menthonnex J.-J., Prat A., Ulrich O., Soldo Y., Trévisson P., Kapoujyan G. and Perroux G. (2005) FAME: a new beamline for X-ray absorption investigations of very-diluted systems of environmental, material and biological interests. *Phys. Scr.* **2005**, 970.

Ram R., Becker M., Brugger J., Etschmann B., Burcher-Jones C., Howard D., Kooyman P. and Petersen J. (2019) Characterisation of a rare earth element (REE)-bearing ion-adsorption clay deposit in Madagascar. *Chem. Geol.* **522**, 93–107.

Ravel B. and Newville M. (2005) ATHENA, ARTEMIS, HEPHAESTUS: data analysis for X-ray absorption spectroscopy using IFEFFIT. *J. Synch. Radiat.* **12**, 537–541.

Richens D. T. (2005) Ligand substitution reactions at inorganic centers. *Chem. Rev.* **105**, 1961–2002.

Rehr J. J., Kas J. J., Prange M. P., Sorini A. P., Takimoto Y. and Vila F. (2009) Ab initio theory and calculations of X-ray spectra. *C.R. Phys.* **10**, 548–559.

Rehr J. J., Kas J. J., Vila F. D. and Newville M. (2017) Theory and Analysis of XAFS. In *XAFS Techniques for Catalysts, Nanomaterials, and Surfaces* (eds. Y. Iwasawa, K. Asakura and M. Tada). Springer, Cham, doi: 10.1007/978-3-319-43866-5_2.

Rodinger T., Howell P. L. and Pomès R. (2005) Absolute free energy calculations by thermodynamic integration in four spatial dimensions. *J. Chem. Phys.* **123** 034104.

Roy M., Gurman S. and Van Dorssen G. (1997) The amplitude reduction factor in EXAFS. *J. Phys.* **IV 7**, C2-151–C152-152.

Rudolph W. W. and Irmer G. (2015) Hydration and ion pair formation in common aqueous La(III) salt solutions – a Raman scattering and DFT study. *Dalton Trans.* **44**, 295–305.

Sharps J. A., Brown G. E. and Stebbins J. F. (1993) Kinetics and mechanism of ligand exchange of Au (III), Zn(II), and Cd(II) chlorides in aqueous solution: An NMR study from 28–98°C. *Geochim. Cosmochim. Acta* **57**, 721–731.

Sheard E. R., Williams-Jones A. E., Heiligmann M., Pederson C. and Trueman D. L. (2012) Controls on the concentration of zirconium, niobium, and the rare earth elements in the Thor lake rare metal deposit, northwest territories, Canada. *Econ. Geol.* **107**, 81–104.

Shock E. L. and Helgeson H. C. (1988) Calculation of the thermodynamic and transport properties of aqueous species at high pressures and temperatures: correlation algorithms for ionic species and equation of state predictions to 5 kb and 1000 °C. *Geochim. Cosmochim. Acta* **52**, 2009–2036.

Skirrow R., Huston D., Mernagh T., Thorne J., Dulfer H. and Senior A. (2013) Critical commodities for a high-tech world: Australia's potential to supply global demand. *Camberra: Geoscience Australia*, 126.

Smith L. S. and Wertz D. L. (1975) Solute structuring in aqueous lanthanum(III) chloride solutions. *J. Am. Chem. Soc.* **97**, 2365–2368.

Smith L. S. and Wertz D. L. (1977) On the coordination of La3+ in aqueous LaBr 3 solutions. *J. Inorg. Nucl. Chem.* **39**, 95–98.

Smith M. P. and Henderson P. (2000) Preliminary fluid inclusion constraints on fluid evolution in the Bayan Obo Fe-REE-Nb deposit, Inner Mongolia, China. *Econ. Geol.* **95**, 1371–1388.

Solera J. A., García J. and Proietti M. G. (1995) Multielectron excitations at the L edges in rare-earth ionic aqueous solutions. *Phys. Rev. B* **51**, 2678–2686.

Sprik M. (1998) Coordination numbers as reaction coordinates in constrained molecular dynamics. *Faraday Discuss.* **110**, 437–445.

Sprik M. and Ciccotti G. (1998) Free energy from constrained molecular dynamics. *J. Chem. Phys.* **109**, 7737.

Sprik M. (2000) Computation of the pK of liquid water using coordination constraints. *Chem. Phys.* **258**(2–3), 139–150.

Stefanski J. and Jahn S. (2020) Yttrium speciation in subduction-zone fluids from ab initio molecular dynamics simulations. *Solid Earth* **11**, 767–789.

Sverjensky D. A., Shock E. L. and Helgeson H. C. (1997) Prediction of the thermodynamic properties of aqueous metal complexes to 1000°C and 5 kb. *Geochim. Cosmochim. Acta* **61**, 1359–1412.

Sverjensky D. A., Harrison B. and Azzolini D. (2014) Water in the deep Earth: The dielectric constant and the solubilities of quartz and corundum to 60kb and 1200°C. *Geochim. Cosmochim. Acta* **129**, 125–145.

Tanger J. C. and Helgeson H. C. (1988) Calculation of the thermodynamic and transport properties of aqueous species at high pressures and temperatures: revised equations of state for the standard partial molal properties of ions and electrolytes. *Am. J. Sci.* **288**, 19–98.

Terrier C., Vitorge P., Gaigeot M.-P., Spezia R. and Vuilleumier R. (2010) Density functional theory based molecular dynamics study of hydration and electronic properties of aqueous La^{3+}. *J. Chem. Phys.* **133** 044509.

Testemale D., Argoud R., Geaymond O. and Hazemann J.-L. (2005) High pressure/high temperature cell for x-ray absorption and scattering techniques. *Rev. Sci. Instrum.* **76** 043905.

Troullier N. and Martins J. L. (1991) Efficient pseudopotentials for plane-wave calculations. *Phys. Rev. B* **43**, 1993–2006.

van Sijl J., Allan N. L., Davies G. R. and Westrenen v. W. (2009) Molecular modelling of rare earth element complexation in subduction zone fluids. *Geochim. Cosmochim. Acta* **73**, 3934–3947.

von Lilienfeld O. A., Tavernelli I., Rothlisberger U. and Sebastiani D. (2004) Optimization of effective atom centered potentials for London dispersion forces in density functional theory. *Phys. Rev. Lett.* **93** 153004.

Williams-Jones A. E., Samson I. M. and Olivo G. R. (2000) The genesis of hydrothermal fluorite-REE deposits in the Gallinas Mountains, New Mexico. *Econ. Geol.* **95**(2), 327–341.

Wood S. A. (1990) The aqueous geochemistry of the rare-earth elements and yttrium: 2. Theoretical predictions of speciation in hydrothermal solutions to 350 C at saturation water vapor pressure. *Chem. Geol.* **88**, 99–125.

Xing Y. L., Mei Y., Etschmann B., Liu W. H. and Brugger J. (2018) Uranium Transport in F-Cl-Bearing Fluids and Hydrothermal Upgrading of U-Cu Ores in IOCG Deposits. *Geofluids* **2018**, 22. Article ID 6835346.

Xing Y. L., Etschmann B., Liu W. H., Mei Y., Shvarov Y., Testemale D., Tomkins A. and Brugger J. (2019) The role of fluorine in hydrothermal mobilization and transportation of Fe, U and REE and the formation of IOCG deposits. *Chem. Geol.* **504**, 158–176.

Zhang Z. and Duan Z. (2005) Prediction of the PVT properties of water over wide range of temperatures and pressures from molecular dynamics simulation. *Phys. Earth Planet. Inter.* **149** (3–4), 335–354.

Zhong R., Li Y., Etschmann B., Brugger J., Yu C. and Cui H. (2020) HighPGibbs, a practical tool for fluid-rock thermodynamic simulation in deep earth and its application on calculating nitrogen speciation in subduction zone fluids. *Geochem. Geophys. Geosyst. (G^3)* **21**(5), 9 pp.

Associate editor: Zoltan Zajacz